Monthly Notices
of the
ROYAL ASTRONOMICAL SOCIETY

MNRAS **437,** 46–66 (2014)
Advance Access publication 2013 October 22

doi:10.1093/mnras/stt1859

Hubble Space Telescope hot Jupiter transmission spectral survey: a detection of Na and strong optical absorption in HAT-P-1b

N. Nikolov,[1]⋆ D. K. Sing,[1] F. Pont,[1] A. S. Burrows,[2] J. J. Fortney,[3] G. E. Ballester,[4] T. M. Evans,[5] C. M. Huitson,[1] H. R. Wakeford,[1] P. A. Wilson,[1] S. Aigrain,[5] D. Deming,[6] N. P. Gibson,[7] G. W. Henry,[8] H. Knutson,[9] A. Lecavelier des Etangs,[10] A. P. Showman,[4] A. Vidal-Madjar[10] and K. Zahnle[11]

[1]*Astrophysics Group, School of Physics, University of Exeter, Stocker Road, Exeter EX4 4QL, UK*
[2]*Department of Astrophysical Sciences, Peyton Hall, Princeton University, Princeton, NJ 08544, USA*
[3]*Department of Astronomy and Astrophysics, University of California, Santa Cruz, CA 95064, USA*
[4]*Lunar and Planetary Laboratory, University of Arizona, Tucson, AZ 85721, USA*
[5]*Department of Physics, University of Oxford, Denys Wilkinson Building, Keble Road, Oxford OX1 3RH, UK*
[6]*Department of Astronomy, University of Maryland, College Park, MD 20742, USA*
[7]*European Southern Observatory, Karl-Schwarzschild-Str. 2, D-85748 Garching bei München, Germany*
[8]*Tennessee State University, 3500 John A. Merritt Blvd., PO Box 9501, Nashville, TN 37209, USA*
[9]*Division of Geological and Planetary Sciences, California Institute of Technology, Pasadena, CA 91125, USA*
[10]*CNRS, Institut dAstrophysique de Paris, UMR 7095, 98 bis boulevard Arago, F-75014 Paris, France*
[11]*NASA Ames Research Center, Moffett Field, CA 94035, USA*

Accepted 2013 September 30. Received 2013 September 30; in original form 2013 July 10

ABSTRACT

We present an optical to near-infrared transmission spectrum of the hot Jupiter HAT-P-1b, based on *Hubble Space Telescope* observations, covering the spectral regime from 0.29 to 1.027 μm with Space Telescope Imaging Spectrograph (STIS), which is coupled with a recent Wide Field Camera 3 (WFC3) transit (1.087 to 1.687 μm). We derive refined physical parameters of the HAT-P-1 system, including an improved orbital ephemeris. The transmission spectrum shows a strong absorption signature shortward of 0.55 μm, with a strong blueward slope into the near-ultraviolet. We detect atmospheric sodium absorption at a 3.3σ significance level, but find no evidence for the potassium feature. The red data imply a marginally flat spectrum with a tentative absorption enhancement at wavelength longer than ∼0.85 μm. The STIS and WFC3 spectra differ significantly in absolute radius level (4.3 ± 1.6 pressure scaleheights), implying strong optical absorption in the atmosphere of HAT-P-1b. The optical to near-infrared difference cannot be explained by stellar activity, as simultaneous stellar activity monitoring of the G0V HAT-P-1b host star and its identical companion show no significant activity that could explain the result. We compare the complete STIS and WFC3 transmission spectrum with theoretical atmospheric models which include haze, sodium and an extra optical absorber. We find that both an optical absorber and a supersolar sodium to water abundance ratio might be a scenario explaining the HAT-P-1b observations. Our results suggest that strong optical absorbers may be a dominant atmospheric feature in some hot Jupiter exoplanets.

Key words: techniques: spectroscopic – planets and satellites: individual: HAT-P-1b – stars: individual: HAT-P-1b.

1 INTRODUCTION

Since the first detection of an exoplanet hosted by a Sun-like star (Mayor & Queloz 1995), the number of extrasolar planets and candidates has rapidly grown, yet exceeding more than 3000. Among them, the planets that temporarily pass in front (transit) or behind (secondary eclipse) the host star offer a unique opportunity to explore their dynamical properties, internal structures and atmospheres (Winn 2010; Seager 2011). Specifically, during transits part of the star light travels through the rarified upper planetary atmosphere (near the terminator) and is partially absorbed by atoms and molecules. This process gives rise to a wavelength dependent variation of the measured transit depth and is central to the method

⋆E-mail: nikolay@astro.ex.ac.uk

of transmission spectroscopy, the subject of this paper. The optical transmission spectrum of a cloud free hot Jupiter exoplanet at temperatures lower than 1500 K is predicted to be dominated by pressure-broadened sodium (Na I) and potassium (K I) resonance lines (Seager & Sasselov 2000; Brown et al. 2001; Burrows et al. 2010; Fortney et al. 2010).

Currently, observations have led to mixed detections of both strong alkali features in several exoplanets with HD 209458b and HD 189733b remaining among the two most studied exoplanets, due to the prominent brightness of their host stars ($V \sim 8$ mag) and deep transit signals. In particular, the optical transmission spectrum of HD 209458b shows broad sodium feature and a lack of potassium (Charbonneau et al. 2002; Narita et al. 2005; Sing et al. 2008b; Snellen et al. 2008). The complete optical to near-infrared spectrum of HD 189733b is described by an increasing planetary radius with decreasing wavelength, most likely due to Rayleigh scattering (Lecavelier Des Etangs et al. 2008; Pont et al. 2008; Sing et al. 2009, 2011b) and presence of narrow line cores of sodium peaking above the slope (Redfield et al. 2008; Huitson et al. 2012; Jensen et al. 2012). Although there is no reason to expect that these two atmospheres should be similar, as infrared observations indicate that the atmosphere of HD 209458b has a temperature inversion (Burrows et al. 2007; Knutson et al. 2008) while the atmosphere of HD 189733b does not (Grillmair et al. 2007; Charbonneau et al. 2008), the significant difference between both planetary atmospheres indicates that clouds and hazes can be very important in determining the overall shape of transmission spectra. In addition to HD 209458b and HD 189733b, a sodium core has also been detected in WASP-17b but with an absorption depth much less than the theoretical prediction (Wood et al. 2011; Zhou & Bayliss 2012). Wood et al. (2011) speculate that the depleted sodium abundance could be due to photoionization. Notably, XO-2b is the first exoplanet for which both sodium and potassium absorption was detected (Sing et al. 2011a, 2012). Unlike HD 189733b, this planet shows no evidence for high-altitude clouds or hazes.

Motivated by the recent observational results and theoretical predictions of strong alkali absorption features, stratosphere inducing TiO and sulphur bearing molecular features, near-infrared molecular features, clouds, hazes and dust we initiated an optical to near-infrared spectroscopic survey of eight close-in giant exoplanets across different regimes of planetary temperature (in the range 1080−2800 K). The ultimate aim of the programme is to classify the monitored targets based on their atmospheric specificity, i.e. clear/hazy, presence/lack of TiO/alkali and other molecular features. Accumulating a large number of observed planets will open the possibility to measure correlations between atmospheric properties and other parameters such as stellar activity and stellar type. In this paper, we report results from three new transit observations of HAT-P-1b with the G430L and G750L gratings of the Space Telescope Imaging Spectrograph (STIS) aboard the *Hubble Space Telescope (HST)*. In addition, we complement our spectroscopic data with the recently reported *HST*/Wide Field Camera 3 (WFC3) G141 transit of Wakeford et al. (2013) and investigate the complete optical to near-infrared transmission spectrum of HAT-P-1b with theory of giant exoplanet atmospheres.

This paper is organized as follows. Section 2 presents the instrument set-up employed for the transit observations and the data reduction. Section 3 describes the data analysis, including a refinement of the system parameters and the construction of the transmission spectrum of HAT-P-1b. Finally, we discuss the results and conclude in Sections 4 and 5, respectively.

1.1 The hot Jupiter HAT-P-1b

Detected by the small automated telescopes of the HATNet ground-based transit survey (Bakos et al. 2007) HAT-P-1b is a giant ($R_p \sim 1.2\,R_J$), low-mean density ($\rho_p \sim 0.4\,\mathrm{g\,cm^{-3}}$) transiting extrasolar planet in a visual binary system, composed of two sun-like stars (separated by angular distance of 11 arcsec on the sky, corresponding to a linear distance of ∼1500 au) located more than 450 light-years away in the northern constellation Lacerta. The host star (HAT-P-1 also known as ADS 16402 A, BD+37 4734, $\alpha = 22^h57^m46\overset{s}{.}8$, $\delta = +38^\circ40'28''$, J2000.0) is a moderately bright G0V dwarf ($V = 10.4$ mag) allowing for characterization follow-up studies. Although it has been suggested by Bakos et al. (2007) that HAT-P-1b is too large to be explained by theoretical models of giant exoplanets, Winn et al. (2007) improved the accuracy of the system parameters of HAT-P-1 and its planet and concluded that the planet radius is in accord with theoretical models of irradiated, coreless, solar-composition giant planets. Furthermore, Johnson et al. (2008) combined Keck I/HIRES[1] and *Subaru*/HDS[2] optical spectra with photometry, detecting the Rossiter–McLaughlin effect and measuring a close alignment between the planet's orbital inclination and the rotation axis of the star $\lambda = 3\overset{\circ}{.}7 \pm 2\overset{\circ}{.}1$. Liu, Burrows & Ibgui (2008) re-examined the core mass needed for HAT-P-1b, compared to the available measurements of its radius at the time and concluded that their inferred core masses are roughly consistent with the stellar metallicity versus core-mass relationship.

The atmosphere of the planet has also been probed with secondary eclipse observations. Todorov et al. (2010) reported *Spitzer*/IRAC[3] photometry of HAT-P-1b during two secondary eclipse observations, covering broad-bands at 3.6, 4.5, 5.8 and 8 μm. The authors found best fits for their results of the secondary eclipse depths using an atmosphere with a modest temperature inversion, intermediate between the archetype inverted atmosphere of HD 209458b and a model without an inversion. Further in their discussion, the authors speculated that the best fit for the average dayside temperature of HAT-P-1b is 1500 ± 100 K. Analysis of the secondary eclipse led the authors to the conclusion that the orbit of HAT-P-1b is close to circular, with a 3σ limit of $|e\cos\omega| < 0.002$. Recently, Béky et al. (2013) reported visible-light *HST*/STIS relative photometry during two occultations of HAT-P-1b, allowing them to constrain the geometric albedo of the planet. Comparing two techniques: (i) relative photometry (of HAT-P-1 A with respect to its companion HAT-P-1 B) and (ii) the traditional steps in removing instrumental artefacts from (single target) *HST* time series, the authors concluded that the second method introduced a strong bias in the albedo result. The authors estimated a 2σ upper limit of 0.64 for the geometric albedo of HAT-P-1b between 5770 and 9470 Å.

2 OBSERVATIONS AND CALIBRATIONS

We obtained low-resolution optical to near-infrared spectra of HAT-P-1 with the STIS instrument aboard the *HST* (Proposal ID GO-12473, PI: Sing) during three transits on UT 2012 May 26 and 30 with grating G430L and 2012 September 19 with grating G750L. Table 1 exhibits a summary of our observations.

Each visit consisted of five ∼96 min orbits, during which data collection was truncated with ∼45 min gaps due to Earth occultations. Given the moderate brightness of HAT-P-1 ($V = 10.4$ mag)

[1] High Resolution Echelle Spectrometer.
[2] High Dispersion Spectrograph.
[3] Infrared Array Camera.

Table 1. *HST* STIS observing dates, instruments and settings.

UT date 2012	Visit number	Optical element	Number of spectra	Integration time (s)
May 26	7	G430L	43	284
May 30	20	G750L	43	284
September 19	8	G430L	43	284

the integration time was set to 284 s to achieve a high signal-to-noise ratio (SNR), resulting in 43 spectra during each visit. Each of the G430L and G750L optical elements possesses a resolving power of $R = 500$, which secures a combined wavelength coverage from 2892 to 10270 Å with a small overlap region between them from 5240 to 5700 Å (see Fig. 1). Similar to Sing et al. (2011a), the data for this study were collected with a wide 52 × 2 arcsec slit to minimize slit losses. Data acquisition overheads were minimized by reading out a reduced portion of the CCD with a size of 1024 × 128.

Each of the three visits consisted of five orbits during which nine spectra were collected. Three of the orbits at each visit were scheduled to provide out of transit (oot) measurements to secure a stable baseline flux while two orbits occurred during the transit events. Therefore, when combined the three visits provide an almost complete light curve, needed for an accurate measurement of the system parameters and the planet radius.

The data were reduced (bias, dark and flat corrected) using the latest version of the `CALSTIS`[4] pipeline and the relevant up-to-date calibration frames.

STIS observations with the G750L grating are prone to significant fringing at wavelengths longward of ∼7000 Å, which can limit the SNR of the derived spectra (Goudfrooij et al. 1998a). The fringes are caused by interference of multiple reflections between the two surfaces of the thinned, backside-illuminated SITe CCD onboard STIS. Although the fringe pattern may have a negligible effect on transmission spectra, acquired from broad spectral widths (∼1000 Å), as pointed out by Knutson et al. (2007) in their analysis of HD 209458b, the effect may be significant at smaller band widths and requires a careful treatment of the fringe pattern on each of the G750L science spectra.

We corrected the fringe pattern present on each of the G750L science spectra of the time series, using a contemporaneous fringe flat image (FFI) and the recipe of Goudfrooij & Christensen (1998b). To summarize, we removed the low order lamp vignetting and normalized the FFI. We then aligned and scaled the infrared fringes to match the fringe pattern of the star spectrum on each of the science spectra. Finally, the stellar spectrum was divided by the shifted flat, to correct for the fringe pattern (see Fig. 1 for a comparison between an original G750L spectrum, exhibiting fringe effect to its defringed version).

2.1 Cosmic ray correction

An examination of the spectral time series showed a high number of recorded cosmic ray (CR) events. This is not unusual given the relatively long integration time of 284 s, employed for our study on HAT-P-1b. For comparison, previous studies on transiting exoplanets with STIS in a low-resolution mode, such as Knutson et al. (2007) on HD 209458 ($V = 7.65$) and Sing et al. (2011b) on HD 189733 ($V = 7.67$ mag), used integration times of ∼20 and ∼64 s, respectively. The application of such shorter integration times (i.e. factor of ∼14 and ∼4 for the aforementioned studies compared to ours) on bright target stars serves to secure time series of spectra with a lower number of CR events and good sampling of the resulting light curves. When recorded on time series of 2D spectra, the CRs act to effectively increase (though 'artificially') the flux of the targeted star on random locations within a limited area along the spectra, and appear as outlier data points on the light curves originating from the affected wavelength bins. We therefore consider the CRs present in our data as a potential source of light-curve systematics and undertook a careful analysis aiming CR identification and correction on the science 2D spectra.

Initially, we aimed to perform the data analysis utilizing the `.crg` images produced after a CR identification and correction by `CALSTIS`. However, it was found in the subsequent analysis that for most of the spectra the CR identification was inadequate. In particular, large portions or in several cases complete lines around the central regions of the spectra were found to be marked as affected by CR events lacking a justification when compared to the original spectrum. We therefore developed an alternative customized method to (i) perform a more efficient CR identification and (ii) to correct the affected regions of the spectra. To identify the CRs on each image, we inspected difference images, constructed from the elements of the time series. First, we computed the differences between each image we aimed to correct for CRs and four neighbouring images: two consecutive images obtained before and two after the image we aim to correct. In this process, each of the resulting four difference images was dominated by a three-component signal. The first and the second major components were determined by the CR events specific for the neighbour image itself and the CRs that were present on the image we aim to correct. The third component was a negligible residual of the stellar spectrum due to variations associated with the observed target (e.g. transits or other short-time-scale events) and/or instrumental systematics (e.g. temperature variations of the telescope). We eliminated the first component, and dramatically reduced the amplitude of the third, after a computation of the median of the four difference images, which resulted in an image containing the CR events only. The later property of the median-combined image allowed us to identify CRs even at locations quite close to the peak of the stellar point spread function (PSF).

To identify the pixels affected by CRs on each median-combined image, we scanned each of the CCD's 128 lines, using a window centred on the pixel we were inspecting. The window had a size of 20 pixels, determined by the typical size of a CR on the detector. We compared the value of the central pixel in the window with the median value of all pixels within the window and flagged central pixels that were found to be 5σ above the median level (where σ is the standard deviation of the examined line pixel values). To flag huge regions of the spectra affected by CRs (i.e. regions with size exceeding the window size), we also compared the central pixel values with the median value of the entire line and again flagged pixels that showed values higher than 5σ above the median level for that line. Next, we used all flagged pixels and computed a nominal PSF profile for each column, using five neighbour columns (ignoring the CR affected pixels in them) before and after the examined column. We then scaled the nominal column to match the one with affected pixels. Finally, all flagged pixels were replaced with their corresponding values in the scaled profile. Following this procedure, we found that the total number of pixels affected by CR events comprise ∼5 per cent of the total number of pixels on the

[4] `CALSTIS` comprises software tools developed for the calibration of STIS data (Katsanis & McGrath 1998) inside the Image Reduction and Analysis Facility (IRAF; http://iraf.noao.edu/) environment.

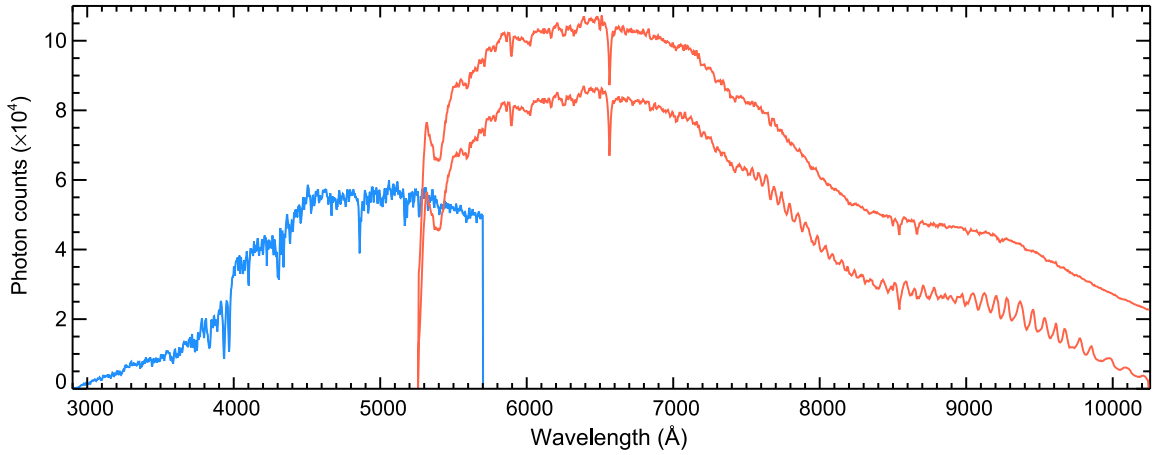

Figure 1. Typical 1D G430L (blue line) and G750L (red line) spectra of HAT-P-1 extracted from our time series. Optical element G430L covers the wavelength range from 2892 to 5700 Å, while G750L spans the range from 5240 to 10270 Å, enabling a construction of the complete optical to near-infrared transmission spectrum of extrasolar planets at low resolution. Note the strong long wavelength fringing beyond ∼7000 Å in grating G750L (displayed on the lower red spectrum) compared to a fringe-corrected data (displayed in the upper red spectrum shifted by 2×10^4 counts for clarity).

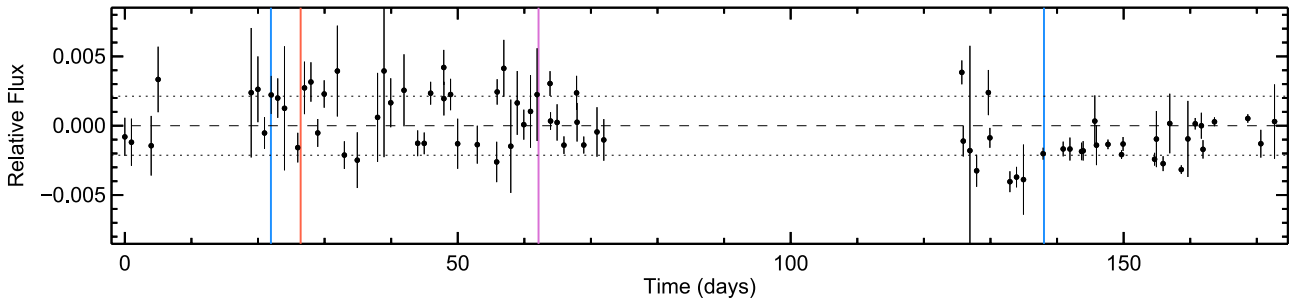

Figure 2. HAT-P-1b stellar variability monitoring performed with the 2.5 m LT spanning 223 d starting UT 2012 May 4. *HST*/STIS G430L, G750L and *HST*/WFC3 G141 visits are indicated with blue, red and purple vertical lines, respectively. The dashed and the two dotted lines indicate the mean and the standard deviation values of the stellar flux.

science images. In addition, we also substituted all pixels identified by `CALSTIS` as 'bad' with the same procedure.

2.2 Stellar variability monitoring

We used the RISE[5] camera on the 2.5 m Liverpool Telescope (LT) at the Roque de los Muchachos Observatory in La Palma, Canary Islands to monitor the brightness of HAT-P-1 for evidence of stellar variability (see Fig. 2). Commencing on UT 2012 May 4 and ending on UT 2012 December 13, the observations spanned a period of 223 d that included the three STIS visits and the WFC3 visit. A series of 300 exposures with integration times of 0.8 s were taken each night with 2 × 2 pixel binning.[6] The telescope was slightly defocused to prevent saturation of the detector and to spread the light across a larger number of pixels and minimize flat fielding errors.

Standard IRAF[7]/PHOT routines were used to obtain accurate centres and perform aperture photometry for HAT-P-1 and three other bright stars within the RISE camera's 9.2 arcmin × 9.2 arcmin field of view. The defocused PSFs typically had full widths at half-maximum of 10−12 pixels (5.4–6.5 arcsec), so we adopted a radius of 9 pixels for the photometric aperture. Larger aperture radii were not possible, due to the nearby companion to HAT-P-1 separated by only ∼20 pixels (11 arcsec). The sky contribution was estimated by taking the median pixel count within an annulus centred on each star, with an inner edge radius of 30 pixels and a width of 60 pixels.

To correct for night-to-night changes in telluric conditions and the instrumental setup, we used the comparison stars to perform differential photometry for HAT-P-1. We experimented with dividing the raw fluxes for HAT-P-1 by different combinations of the comparison stars' raw fluxes. In the end, however, we only used the nearby bright comparison star, as the others were simply too faint.

2.3 STIS white light curves

Spectral extractions were performed in IRAF using the `APALL` procedure. The photon flux originating from a wavelength range in each spectrum of the time series was summed to produce a light curve for that wavelength bin. Photometric per-point uncertainties were initially derived based on pure photon statistics. Similar to other spectrophotometric studies, we refer to the light curve computed after a summation of the complete wavelength range as 'white' light curve.

An optimum performance of the spectral extraction procedure was secured by a selection of the combination of an aperture size and background subtraction (among various aperture sizes) that minimize the oot root mean square (rms) flux of the resulting white light curve. It was found that the smallest scatter was achieved with

[5] Rapid Imaging Search for Exoplanets (Steele et al. 2008).
[6] Such short integration times are only possible due to the short read-out time of RISE.
[7] IRAF stands for Image Reduction and Analysis Facility.

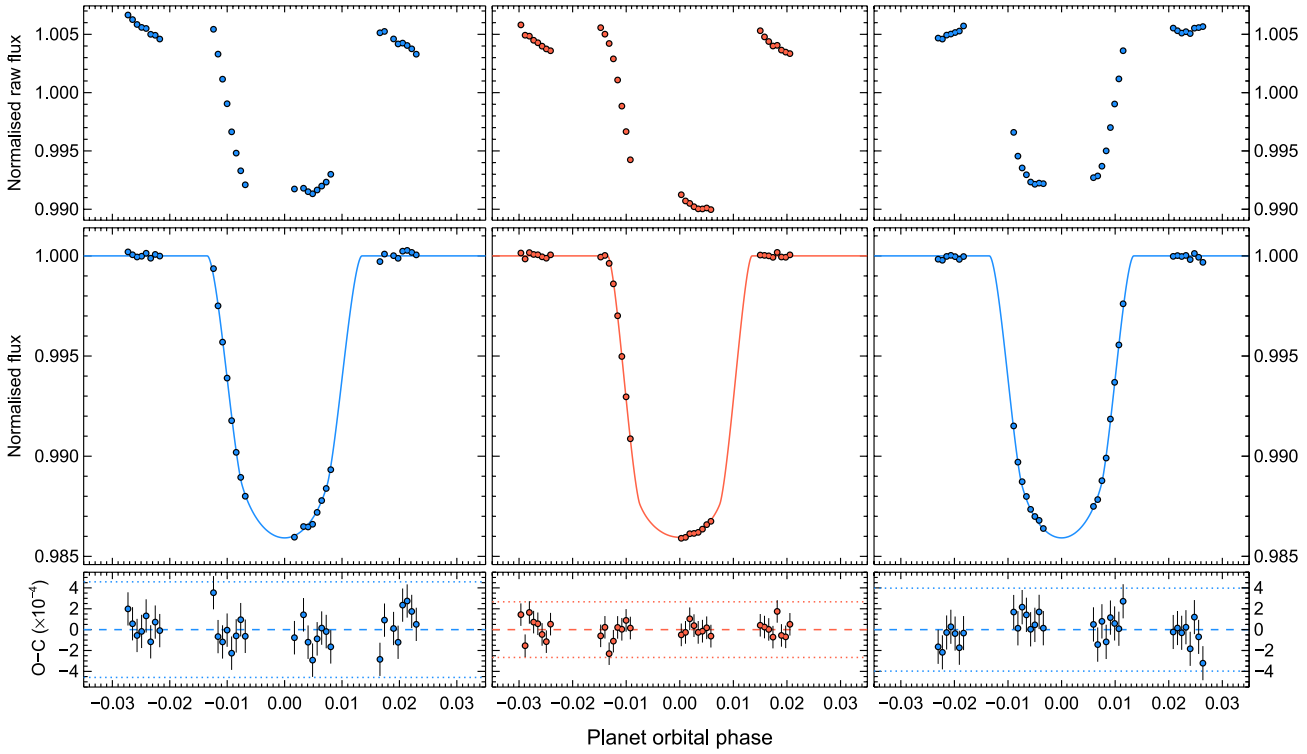

Figure 3. *HST*/STIS normalized white light curves based on data collected during the three visits (left to right): on UT 2012 May 26 (G430L), May 30 (G750L) and September 19 (G430L). Top panels: raw light curves normalized to the mean raw flux (originally in electrons). The light curves experience prominent systematics associated with the *HST* thermal cycle (see the text for details). Middle panels: detrended light curves along with the best-fitting transit model (Mandel & Agol 2002) superimposed with continuous lines. Lower panels: observed minus modelled light-curve residuals, compared to a null (dashed lines) and a 3σ level (dotted lines) used to identify outliers. The spectrophotometric data from G430L and G750L are colour coded in blue and red, respectively.

a 13 pixel wide aperture. A wavelength solution was obtained from the `_x1d` files from `CALSTIS`. Similar to previous *HST*/STIS studies on transiting exoplanets, the first orbit of each transit observation (purposely scheduled earlier than each transit event) as well as the first exposure of each orbit were discarded. That data exhibit complex and unique systematics, as they were acquired while the telescope was thermally relaxing into its new pointing position. Following the aforementioned data quality constraints, each of the three STIS transit observations resulted in four orbits, each of which containing eight measurements (see the top panels of Fig. 3).

2.4 A WFC3 near-infrared complement

Results for HAT-P-1b from an *HST*/WFC3 G141 transit observation (visit 26) in drift scanning mode have been reported by Wakeford et al. (2013). The data comprised of four orbits, each containing ∼45 min intervals of data collection with an integration time of ∼47 s. Notably, the WFC3 field of view also permitted data sampling of the PSF of star HAT-P-1B, which is the second component of the G0V/G0V visual binary that contains the host of HAT-P-1b. Since HAT-P-1B is low active star, it may serve as a comparison star for relative photometry. The white light curve based on the *HST*/WFC3 data was also useful in determining the system parameters of HAT-P-1. We therefore include that light curve in the analysis of the STIS data (see the top panels of Fig. 4).

3 ANALYSIS

A transit light-curve analysis was performed for each visit employing a two-component model fit to the data. The first component is based on the complete analytic transit formula given in Mandel & Agol (2002), which in addition to the central transit times (T_C) and orbital period (P) is a function of the orbital inclination (i), normalized planet semimajor axis (a/R_*) and planet to star radius ratio (R_p/R_*). To account for the limb darkening of HAT-P-1 we employ the four parameter non-linear limb darkening law defined in Claret (2000) given by

$$\frac{I(\mu)}{I(1)} = 1 - \sum_{n=1}^{4} c_n(1 - \mu^{n/2}), \quad (1)$$

where $I(1)$ is the intensity at the centre of the stellar disc and $\mu = \cos\theta$, where θ is the angle between the line of sight and the normal to the stellar surface and c_n, $n = 1, 4$ are the four limb darkening coefficients.

We choose to rely on theoretically derived stellar limb darkening coefficients comparing the data to both `1D` and `3D` stellar models, rather than to fit for them in the data in order to reduce the number of free parameters in the fit (typically four parameters per grating). Furthermore, this approach also eliminates the well-known wavelength-dependent degeneracy of limb darkening with transit depth (Sing et al. 2008a).

Initially, the values for the four limb darkening coefficients were derived from the `1D ATLAS` theoretical stellar models of Kurucz,[8] following the procedures described in Sing (2010). In particular, we obtained theoretical limb darkening coefficients for the closest match to a star with the physical properties of HAT-P-1,

[8] http://kurucz.harvard.edu/

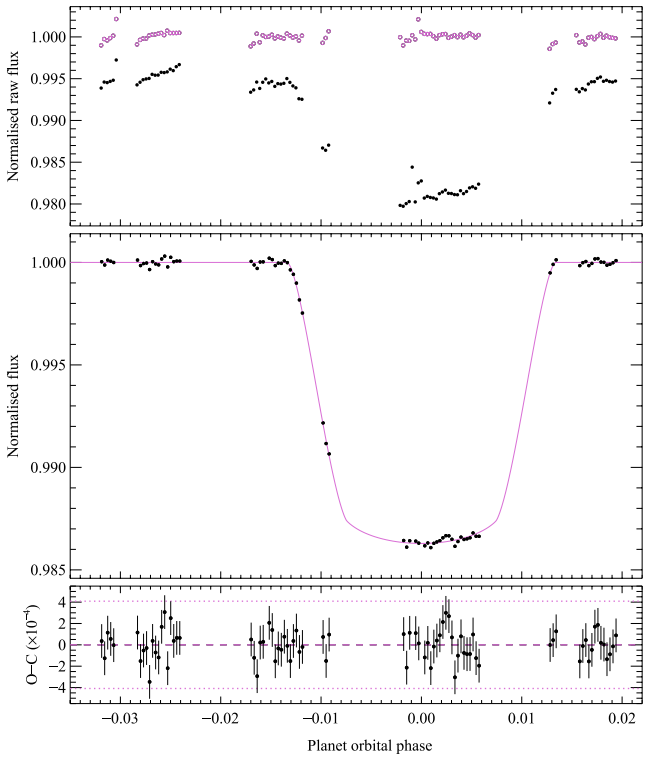

Figure 4. *HST*/WFC3 transit data from Wakeford et al. (2013), included in the simultaneous fit. Top panel: raw white light curves of a comparison star (open circles in purple) and HAT-P-1 (black dots). Middle panel: relative photometry of HAT-P-1 with respect to the comparison star along with the best-fitting transit model (Mandel & Agol 2002) displayed with a purple line. Lower panel: observed minus computed residuals. The 3σ residual rms levels are indicated with dotted lines compared to zero level.

i.e. $T_{\rm eff} = 6000$ K, $\log g = 4.5$ and [Fe/H] = 0.0. Previous analyses on high SNR transit light curves with limb darkening coefficients derived from 1D model predictions sometimes resulted in poor fits, especially in the ingress and egress phases of the transit, which is characteristic of incorrect limb darkening (Hayek et al. 2012). The main reason for this issue lies in a generic shortcomings in the structure of 1D model atmospheres compared to more sophisticated 3D stellar atmospheric models. In particular, when compared in the case of the solar atmosphere, 3D models explicitly take into account the effect of convective motions in the surface granulation and reproduce the solar atmosphere with a higher degree of realism. Hayek et al. (2012) employed 3D stellar atmospheric models and computed limb darkening coefficients for HD 209458. Notably, the stellar atmospheric parameters of HAT-P-1 are quite similar (at the 1σ level) to those of HD 209458 as displayed in Table 2. In particular, both stars are of similar effective temperature, however, HD 209458 is 120 K hotter than HAT-P-1. That difference however, is well within the effective temperature uncertainties of both stars, which allows one to adopt the available HD 209458 limb darkening coefficients in the analysis of HAT-P-1. We compare both the 1D and 3D models in the forthcoming analysis sections.

Table 2. Spectroscopically derived stellar atmospheric parameters for HD 209458 and HAT-P-1.

Property	HD 209458 Hayek et al. (2012)	HAT-P-1 Torres, Winn & Holman (2008)
$T_{\rm eff}$, K	6095 ± 53	5975 ± 120
$\log g$, cm s^{-2}	4.30 ± 0.09	4.45 ± 0.15
[Fe/H], dex	0.00 ± 0.04	0.13 ± 0.08

Previous STIS data analyses showed that the first integration exhibits abnormally low flux (Charbonneau et al. 2002; Pont et al. 2008; Sing et al. 2008b, 2011a; Huitson et al. 2012). We attempted to resolve this issue by incorporating an additional 1 s long exposure prior to the 284 s integrations. However, it has been found that skipping the 1 s and the first 284 s integration of each orbit improved the fit by reducing the χ^2 value. We therefore exclude these two data points from each orbit in the analysis.

The raw STIS light curves exhibit instrumental systematics similar to those described by Gilliland, Goudfrooij & Kimble (1999) and Brown et al. (2001). In summary, the major source of the systematics is related with the orbital motion of the telescope. In particular, the *HST* focus is known to experience quite noticeable variations on the spacecraft orbital time-scale, which are attributed to thermal contraction/expansion (often referred as the 'breathing effect') of the optical telescope assembly as the telescope warms up during its orbital day and cools down during orbital night (Hasan & Bely 1993, 1994; Suchkov & Hershey 1998). We take into account the systematics associated with the telescope temperature variations in the transit light-curve analysis using a baseline function, which we multiply to the transit model in flux. Similar to past STIS studies, the main ingredient of the baseline function is a polynomial of fourth degree of the *HST* orbital phase (ϕ_t). In addition, we find in the light-curve analysis that the systematics vary from orbit to orbit (i.e. dependence with time, t), which is a known effect from previous STIS studies as well as the detector positions of the spectra, as determined by the spectral trace orientation (x, y) obtained from the APPAL task in IRAF and the shift (ω) of each spectrum of the time series, compared to a reference (i.e. cross-correlated typically with the first spectrum). Model selection was further investigated including (i) polynomials of degrees higher than fourth order for the *HST* orbital phase and (ii) additional terms to the planet orbital phase, spectral shifts and traces. However, those models were found statistically unjustified for this particular data set and hence rejected based on the Bayesian Information Criterion (BIC) introduced by Schwarz (1978):

$$\mathrm{BIC} = \chi^2 + k \ln n, \qquad (2)$$

where k is the number of free parameters and n is the number of data points. A summary of the model selection analysis is presented in Appendix A.

Systematics correction was also performed following the divide out of transit method described in Berta et al. (2012), where a template correction is constructed using the data from the oot orbits. Although the idea would work well for instruments with strictly repeating systematics (such as data from *HST*/WFC3) we found that the resulting oot light-curve rms for our STIS white or binned light curves is a factor of a few higher than the one from the conventional detrending method (adopted in this work). In addition the timing of the *HST* exposures is known to change slightly from orbit to orbit relative to the *HST* orbital phase, which makes the systematics associated with each orbit unique. We therefore chose to remove the systematics using a parametrized fit to the data.

An accurate determination of reliable uncertainties of the system parameters often requires a careful treatment of the photometric uncertainties. Time-correlated or 'red' noise is often present in high precision photometry and can influence the final parameter determination. To investigate the noise in our light curves, we

Table 3. 3D limb darkening coefficients employed in the simultaneous fit and results for the fitted R_p/R_* and the residual scatter in parts per million (ppm).

Visit ID	Instrument	c_1	c_2	c_3	c_4	R_p/R_*	rms (ppm)
7	STIS/G430 L	0.4397	0.3754	0.1005	−0.0622	0.11849 ± 0.00046	120
8	STIS/G430 L	0.4397	0.3754	0.1005	−0.0622	0.11849 ± 0.00046	133
20	STIS/G750 L	0.7093	−0.2265	0.3273	−0.1240	0.11808 ± 0.00034	81
26	WFC3/G141	0.6958	−0.3332	0.3787	−0.1267	0.11763 ± 0.00028	182

applied the time-averaging procedure (Pont, Zucker & Queloz 2006; Winn et al. 2009) and binned light-curve residuals in time by n data points. For each light curve, we computed the β-ratio between the rms residual of the binned (σ_N) and unbinned (σ_1) data. In case that the data are free of red noise it is expected that the binned (in M bins) residuals follow the relation

$$\sigma_N = \frac{\sigma_1}{\sqrt{N}}\sqrt{\frac{M}{M-1}}. \quad (3)$$

However, often in reality $\sigma_N \geq \sigma_1$ by the factor β. The β factor is often used to rescale each photometric uncertainty of a data set. Since our data contain only nine data points for each orbit of the four visits in each light curve, it was a difficult task to obtain reliable estimates of the β factor for large bin sizes ($N > 15$). However, we find $\beta \sim 1.3$, 1.2, 1 and 1.4 for the white light curves of visits 7, 8, 20 and the WFC3 white light curve when binning no more than 15 data points.

We determine the best-fitting parameters of the two-component function to the data using the Levenberg–Marquardt least-squares algorithm as implemented in the IDL[9] MPFIT[10] package (Markwardt 2009). The final results for the uncertainties of the fitted parameters were taken from MPFIT after a rescale for any non-unity reduced χ^2 values.

3.1 System parameters and transit ephemeris

One of the goals of the present study is to derive accurate system parameters of HAT-P-1b including an improved transit ephemeris. To achieve this task, ideally one would use a complete and well-sampled transit observation at wavelengths close to or in the infrared, where the stellar limb darkening is minimized and allows accurate parameters to be determined. In this study, we rely on the white light curves to derive system parameters. When combined, these curves span nearly a complete transit, sampled once each 294 s, covering the full optical to near-infrared wavelength rage. While several complete transit light curves have been reported from the ground, we consider the quality of the STIS and WFC3 white light curves as high and the wavelength coverage wide. We therefore, choose to model the four *HST* visits simultaneously.

Furthermore, as the orbital inclination (i) and the normalized semimajor axis (a/R_*) should not depend on the observed passband, we treat these parameters in our fitting code as single values and fit for all transit mid-times (T_C), planet to star radius ratios (R_p/R_*) and the coefficients responsible for the light-curve systematics separately for each visit. In addition, we also fit R_p/R_* to a common value for the two G430L gratings. At each run, we used the derived three transit mid-times and complemented them with all available transit times reported in the literature (with number of transit times indicated in parenthesis after the authors), namely the transit times reported in Bakos et al. (2007) (1), Johnson et al. (2008) (7) and Winn et al. (2008) (2) and fitted a linear ephemeris of the form

$$T_C(E) = T_0 + E \times P, \quad (4)$$

where T_C is the central time at each observation, T_0 is the reference transit time and E and P are the transit epoch and period, respectively.

The result for the orbital period was then used as an initial guess for a new run. The complete process was iterated until a convergence for the value of the orbital period. Although we used the system parameters reported in Johnson et al. (2008) as initial guesses for the first run of our code, we found that MPFIT is generally insensitive to the initial guess, except the cases when the starting values significantly differ from the actual ones.

We followed the aforementioned procedure and also investigated the results for all system parameters using the four limb darkening coefficients from the 1D and 3D atmospheric modelling. Generally, both approaches provided results in good agreement (at the one sigma level) with a χ^2 value slightly smaller (<6 per cent) for the derived parameters using the 3D limb darkening coefficients. Our best-fitting model gave $a/r_* = 9.853 \pm 0.071$, $i = 85.^{\circ}634 \pm 0.^{\circ}056$, $\rho_* = 0.908 \pm 0.020$ g cm^{-3}. Table 3 summarizes the limb darkening coefficients used for each data set as well as the results for R_p/R_*. The best-fitting models and detrended light curves for the three STIS and WFC3 white light curves are presented in Figs 3 and 4. We note that the systematics model identified individually for each white light curve differed from the ones identified from the joint fit of the four data sets. In the joint fit, the BIC was minimized for all STIS and WFC3 white light curves when we input models 4 and 3 from Table A1, respectively. As the results for i, a/R_* and R_p/R_* were found to be within one sigma for each model, similar to those for the individual white light curves, as summarized in Table A1 we adopted models 4 and 2 and report the final white light-curve fit result according to them.

For the transit ephemeris, we find the following results for the reference transit time and orbital period, respectively:

$$T_0 = 245\,3979.932\,02 \pm 0.000\,24 \text{ BJD}, \quad (5)$$

$$P = 4.465\,299\,76 \pm 0.000\,000\,55 \text{ d}. \quad (6)$$

The fit resulted in $\chi^2 = 13.36$ with 12 degrees of freedom (i.e. $\chi^2_r = 1.11$), indicating a constant period. A plot of the observed minus computed transit times is displayed in Fig. 5. We find no significant transit timing anomalies at a few minutes level. All transit times are reported in Table 4 for convenience. We find overall agreement between the derived system parameters of HAT-P-1 in this work and the most recent results available in the literature. Torres, Andersen & Giménez (2010) performed a uniform analysis of all ground-based transit light curves coupled with the observable

[9] IDL stands for Interactive Data Language.
[10] http://www.physics.wisc.edu/~craigm/idl/fitting.html

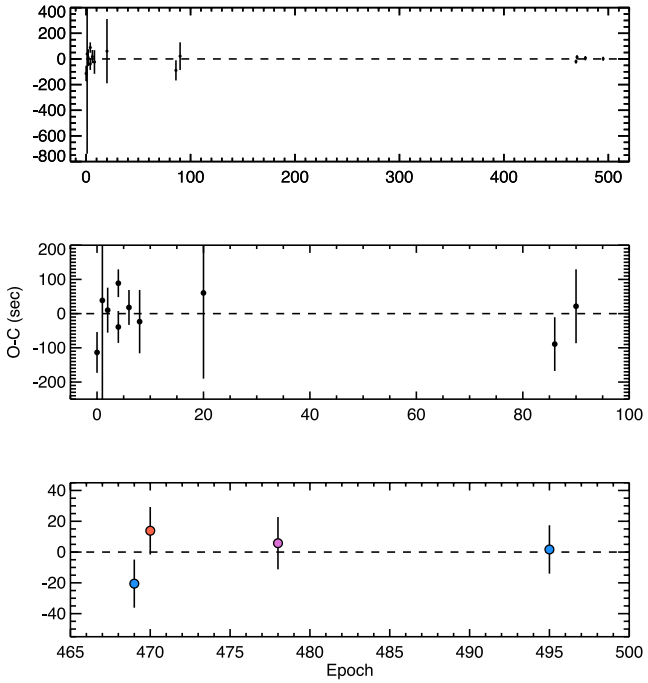

Figure 5. Top panel: observed minus computed (O−C) diagram for HAT-P-1b after a combined analysis of previous transit observations with the three transits presented in this work. Middle panel: a zoom around the first group of data points. Lower panel: a magnification around the three central times reported in this work and the WFC3 measurement of Wakeford et al. (2013), colour coded with blue (G430L), red (G750L) and purple (G141).

Table 4. Transit mid-times obtained from previous studies of HAT-P-1 along with the three measurements of T_C acquired from the *HST*/STIS data. The observed minus computed (O−C) residuals have been derived from a linear fit to the transit mid-times.

Epoch	Central time (BJD$_{TDB}$)	O−C (d)	Reference
0	245 3979.930 71 ± 0.000 69	− 0.001 313	2
1	245 3984.3978 ± 0.0090	0.000 447	1
2	245 3988.862 74 ± 0.000 76	0.000 118	2
4	245 3997.792 77 ± 0.000 54	− 0.000 452	2
4	245 3997.794 25 ± 0.000 47	0.001 028	2
6	245 4006.724 03 ± 0.000 59	0.000 208	2
8	245 4015.6541 ± 0.0011	− 0.000 272	2
20	245 4069.2387 ± 0.0029	0.000 700	2
86	245 4363.946 77 ± 0.000 91	− 0.001 031	3
90	245 4381.8092 ± 0.0013	0.000 249	3
469	245 6074.157 37 ± 0.000 18	− 0.000 238	4
470	245 6078.623 07 ± 0.000 18	0.000 160	4
478	245 6114.345 37 ± 0.000 20	0.000 067	4
495	245 6190.255 42 ± 0.000 18	0.000 019	4

Reference: 1 −Bakos et al. (2007); 2 −Winn et al. (2007); 3 − Johnson et al. (2008) and 4 −this work.

spectroscopic properties of HAT-P-1 and refined its physical parameters. For the main quantities that originate from a pure light-curve fit: orbital inclination (i), normalized semimajor axis (a/R_*) and stellar density (ρ_*) our results differ with those of Torres et al. (2010) at the $\sim 2\sigma$ level. Notably the absolute values for all of the three parameters are below the values reported in Torres et al. (2010). Our measurements, however, have much smaller uncertainties as they originate from a joint analysis of four transit observations, covering a complete transit, wide wavelength span and much higher precision compared to any of the present ground-based photometric data sets and improve the precision of those quantities by a factor of a few. Finally, we employed limb darkening coefficients derived from a 3D stellar atmospheric models that explicitly take into account convective motions in the stellar surface granulation. That effect is neglected in the computation of limb darkening coefficients in the traditional 1D atmospheric models adopted in the previous analyses of HAT-P-1 data.

When coupled with radial velocity data, transit photometry can provide a list of astrophysical parameters for a given planetary system. We therefore also complemented the STIS and WFC3 white light curves of HAT-P-1 with the existing radial velocity data measurements, reported in Bakos et al. (2007) and Johnson et al. (2008). We excluded the radial velocity data that covers the Rossiter effect, as it is beyond the scope of this work to measure the spin–orbit alignment of HAT-P-1. To perform a joint light curve and radial velocity modelling fit, we employed the publicly available EXOFAST package of Eastman, Gaudi & Agol (2012), which incorporates a Markov chain Monte Carlo analysis of the fitted parameters and uncertainties. EXOFAST also served as an independent test for the propriety of our results and especially of the related uncertainties based on the MPFIT procedure. The physical parameters and the improved ephemeris derived from the joint fitting with MPFIT served as priors for EXOFAST. This assumption is necessary because of a limitation in EXOFAST that requires one to input a single band light curve in addition to the radial velocity data. Furthermore, we also modified the code to take into account the four parameter non-linear limb darkening law instead of the currently available two-parameter quadratic limb darkening law. In addition, EXOFAST utilizes the Torres et al. (2010) empirical polynomial relation between the masses and radii of stars, and their surface gravity ($\log g$), effective temperatures ($T_{\rm eff}$) and metallicities [Fe/H], based on a large sample of non-interacting binaries with accurately measured astrophysical parameters. The empirical relation hence allows a derivation of a complete list of orbital and physical properties based on a joint analysis of transit photometric and velocity data (Eastman et al. 2012). We modelled each of the blue, red and near-infrared white light curves independently, except both STIS G430L curves which we fit simultaneously, as they originate from one band. We included the same models for the systematics as in the MPFIT analysis. The final results of all parameters represent the average values from the three fits, except those for i, a/R_* and $R_{\rm p}/R_*$, which were computed using a weighted mean (as the EXOFAST values were found in good agreement with the MPFIT result and because we used four multi-epoch data sets). The transit ephemeris was derived using the approach described at the beginning of this section. Table 5 summarizes our final results.

3.2 Transmission spectra fits

The primary science goal of this project was to construct a low-resolution optical to near-infrared transmission spectrum of HAT-P-1b and to pursue the prediction of strong optical absorbers such as sodium (observed through the (Na I doublet at $\lambda = 5893$ Å), potassium and water vapour or alternatively optical high-altitude atmospheric hazes, gradually enhancing the absorption as a function of decreasing wavelength (i.e. $\lambda < 6000$ Å) in the planetary atmosphere. To construct the complete transmission spectrum, we

Table 5. System parameters for HAT-P-1b and its hosts star based on the STIS, WFC3 and radial velocity data.

Symbol	Parameter and Units	Value
Stellar parameters		
M_*	Mass ($M_\odot$)	$1.151^{+0.052}_{-0.051}$
R_*	Radius ($R_\odot$)	$1.174^{+0.026}_{-0.027}$
L_*	Luminosity ($L_\odot$)	$1.585^{+0.099}_{-0.094}$
ρ_*	Density (cgs)	$0.908^{+0.019}_{-0.022}$
$\log(g_*)$	Surface gravity (cgs)	$4.359^{+0.014}_{-0.014}$
$T_{\rm eff}$	Effective temperature (K)	5980^{+49}_{-49}
[Fe/H]	Metallicity	$0.130^{+0.008}_{-0.008}$
Planetary parameters		
P	Period (d)	$4.465\,299\,76 \pm (55)$
a	Semimajor axis (a)	$0.055\,61^{+0.00082}_{-0.00083}$
M_P	Mass (M_J)	$0.525^{+0.019}_{-0.019}$
R_P	Radius (R_J)	$1.319^{+0.019}_{-0.019}$
ρ_P	Density (cgs)	$0.282^{+0.010}_{-0.009}$
$\log(g_P)$	Surface gravity	$2.873^{+0.010}_{-0.010}$
T_{eq}	Equilibrium temperature (K)	1322^{+14}_{-15}
Θ	Safronov number	$0.0384^{+0.0012}_{-0.0012}$
$\langle F \rangle$	Incident flux (10^9 ergs^{-1}cm^{-2})	$0.699^{+0.032}_{-0.032}$
RV parameters		
K	RV semi-amplitude (m s^{-1})	$58.9^{+1.2}_{-1.2}$
$M_P \sin i$	Minimum mass (M_J)	$0.524^{+0.019}_{-0.019}$
M_P/M_*	Mass ratio	$0.000\,436^{+0.000011}_{-0.000011}$
Transit parameters		
T_C	Transit time (BJD_{TDB})	$2453\,979.932\,02 \pm (24)$
R_P/R_*	Radius of planet in stellar radii	$0.118\,02^{+0.00018}_{-0.00018}$
a/R_*	Semimajor axis in stellar radii	$9.853^{+0.071}_{-0.071}$
i	Inclination ($^\circ$)	$85.634^{+0.056}_{-0.056}$
b	Impact parameter	$0.7501^{+0.0064}_{-0.0069}$
τ	Ingress/egress duration (d)	$0.023\,24^{+0.00047}_{-0.00047}$
T_{14}	Total duration (d)	$0.118\,75^{+0.00049}_{-0.00053}$

extract light curves from spectral bins from each STIS grating[11] on an individual basis, which enables an independent check for consistency. To perform the light-curve fitting, we rely on the MPFIT procedure and the system parameters derived from the joint analysis of the four white light curves in Section 3.1. In particular, for each light-curve fit, we fix the orbital period (P), inclination (i) and normalized semimajor axis (a/R_*) to their joint values along with the transit mid-times (T_C) in each corresponding grating. Furthermore, we keep the four limb darkening coefficients fixed to their theoretical values. To construct the transmission spectrum in each grating, we fit for R_p/R_* and the parameters describing the instrument systematics in the baseline function.

Model selection was performed for each grating assuming photometric errors based on pure photon noise. Once a given systematics model was selected, we re-estimated common uncertainties for our photometric data points, obtained from each spectral bin (i.e. taking the variance of the light-curve residual). This is reasonable, because all photometric errors are equal in a given spectral bin as is typically the case for space-based observations. For example, we find no evidence in our data for a significant background variation which potentially could cause a variation of the photometric errors.

[11] We refer the reader to Wakeford et al. (2013) for details on the derivation of the WFC3 transmission spectrum.

3.2.1 G430L

To construct the G430L transmission spectrum we produced light curves from spectral bins with custom sizes, common for both visits (7 and 8). Initially, we choose five bins with fixed size (in this case ∼500 Å wide), as in various similar spectrophotometric studies. Although it seems natural to select an integer number and fixed size for the bins rather than various bin sizes, it has been found in the analysis that the light curves at that bin choice exhibited significant differences in the quality, except in the last two reddest bins. This is not surprising as the SNR of the data points in each light curve is correlated with the flux level within the wavelength range, constrained from the borders of each bin in the stellar spectrum and the sensitivity of STIS (see Fig. 1). We therefore choose to construct light curves from custom size bins, yet placing uniform constrain on the SNR of the photometric measurements, as determined naturally by the spectra. Ideally, one would aim to select a bin size such as not to lose too much information of the subsequent transmission spectrum in larger bins, nor to obtain light curves from tiny bins dominated by photon noise. We therefore experimented with various bin sizes, such that the SNR of each light curve was $\sim(2–3) \times 10^3$. Following this approach for both G430L data sets, we constructed five bin sizes, as summarized in Table 6.

We measured the planet to star radius ratio (R_p/R_*) with a fit to the transit light curves originating from each wavelength bin. It has been found during the analysis that light-curve fits with 3D limb darkening coefficients generally result in lower χ^2_r compared to the 1D alternative (typically less than 1–2 per cent). We therefore report the remaining of the analysis based on the 3D limb darkening coefficients. Model selection was performed in two stages: (i) first we used the data from each grating individually and (ii) combined in a simultaneous fit. In the first case, it has been found that the BIC values for all of the competing models were similar without clearly indicated models. The lowest BIC values were obtained when using models 4 and 1 (see Table A1 for details) for visits 7 and 8, respectively. However, it should be pointed out that both transmission spectra originating from the aforementioned models were remarkably similar in shape, i.e. the individual measurements agree within the 1σ error bars. Although both related data sets were obtained at about four months difference (see Table 1), there is no evidence for a difference in the measured average level nor the shape of the transmission spectrum (in terms of R_p/R_*). This is unsurprisingly given the fact that the host star is not found to be active and there is no evidence for spot crossing events, which might cause wavelength dependent transit-depth shifts. A significant exception however, resulted for the measured R_p/R_* based on the bluest bin (2900−3800 Å), where the difference is at $\sim 2\sigma$ level (see Fig. 6 for details). Notably, it was only that measurement that varied with $\sim 2\sigma$ during the model selection stage for visit 7 from its initial value in agreement with the value from visit 8 down to its lowest position (models 1 to 4, respectively). In contrast, the same spectral bin resulted in similar R_p/R_* for visit 8 regardless of the applied systematics model. While we could interpret the described behaviour of the visit 7 data set in the bin range 2900–3800 Å as indicative for unreliable data, we chose not to ignore it

Table 6. Measured R_p/R_* from transit light curves fits and theoretical limb darkening coefficients from 3D stellar atmosphere models.

λ (Å)	R_p/R_*	c_1	c_2	c_3	c_4
Visit 7 and 8					
2900−3800	0.118 51 ± 0.000 75	0.2344	0.6735	0.0508	−0.0574
3800−4300	0.118 54 ± 0.000 52	0.3343	0.4421	0.2378	−0.1260
4300−4800	0.118 45 ± 0.000 35	0.4306	0.4531	0.0111	−0.0289
4800−5240	0.117 76 ± 0.000 34	0.5291	0.2790	0.0639	−0.0424
5240−5700	0.117 09 ± 0.000 34	0.6016	0.1090	0.1561	−0.0686
Visit 20					
5293−5878	0.118 26 ± 0.000 39	0.6153	0.0837	0.1617	−0.0700
5878−5908	0.1223 ± 0.0014	0.6309	0.0098	0.2242	−0.0975
5908−6493	0.117 78 ± 0.000 36	0.6705	−0.0572	0.2281	−0.0913
6500−6900	0.117 82 ± 0.000 49	0.7170	−0.1751	0.2844	−0.1106
6900−7300	0.117 99 ± 0.000 53	0.7246	−0.2432	0.3483	−0.1326
7300−7800	0.118 25 ± 0.000 49	0.7374	−0.3021	0.3787	−0.1421
7800−8500	0.118 17 ± 0.000 50	0.7507	−0.3606	0.4072	−0.1512
8500−9200	0.118 68 ± 0.000 71	0.7502	−0.4111	0.4339	−0.1594
9200−102 00	0.119 88 ± 0.000 46	0.7472	−0.4208	0.4174	−0.1494

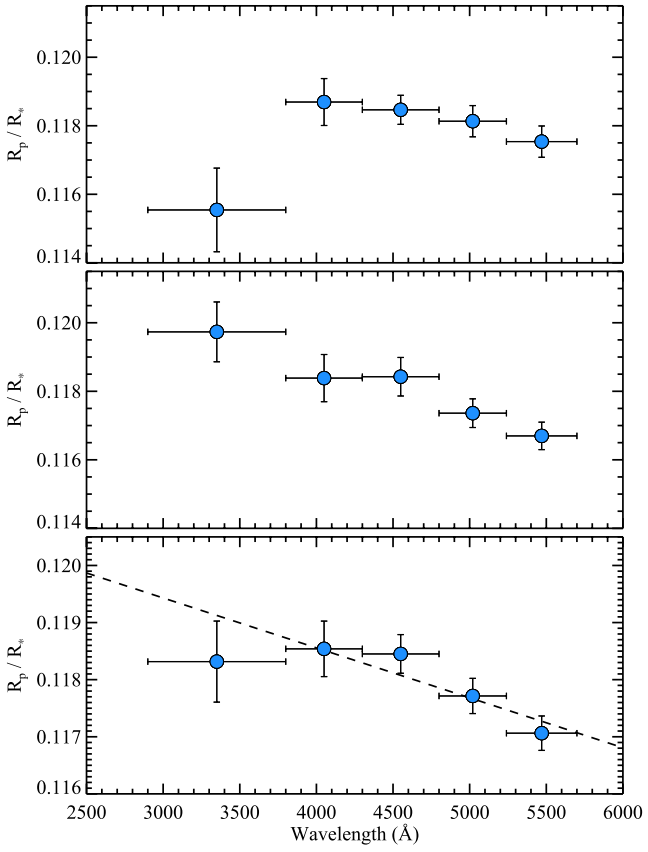

Figure 6. Top panel: STIS G430L transmission spectra based on individual light-curve fits to the data from visit 7. Middle panel: visit 8. Lower panel: weighted mean of visits 7 and 8, compared to a linear fit. The wavelength bin sizes are indicated with horizontal error bars and the 1σ uncertainties for the measured planet to star radius ratio (R_{pl}/R_*) are indicated with vertical error bars.

and proceeded to a simultaneous fit of both visits as the light curves complement each other in phase when taken together.

A simultaneous fit was performed to both blue visits aiming to derive a single value for the planet to star radius ratio (R_p/R_*). We examined again the BIC evolution using the four mentioned systematics models and also included a fifth case, based on the best result from the individual model selection approach. Generally, the transmission spectrum did not change from model to model. Again R_p/R_* measured in the first bin was found to be the most unstable. However, in contrast to the first case, R_p/R_* remained within $\sim 1\sigma$. The lowest BIC value was obtained for case model 5, i.e. models 4 and 1 for visits 7 and 8, respectively. In fact, this result is a confirmation to our previous finding in the individual model selection method. We therefore chose to complete the analysis of the blue part of the STIS transmission spectrum using those models. Finally, to corroborate our results for the G430L transmission spectrum, we also shifted the spectral bins around their present position with 50 Å and examined the resulting transmission spectrum, finding no significant differences (i.e. larger than 1σ). Table 6 and Fig. 7 report our final results. We further display the raw and detrended light curves along with the residuals in Fig. 8.

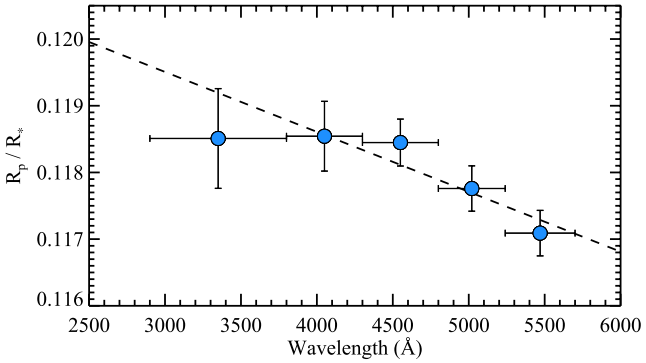

Figure 7. Similar to Fig. 6, but for the joint fit to visits 7 and 8.

3.2.2 G750L

The red STIS data were analysed similar to the blue. Again, we choose custom bin sizes through the complete wavelength region yet aiming to obtain similar SNRs for each light curve in the range $(2-3) \times 10^3$. This approach ensures that each spectral bin produces light curve that is similar in quality to the remaining light curves from the entire grating.

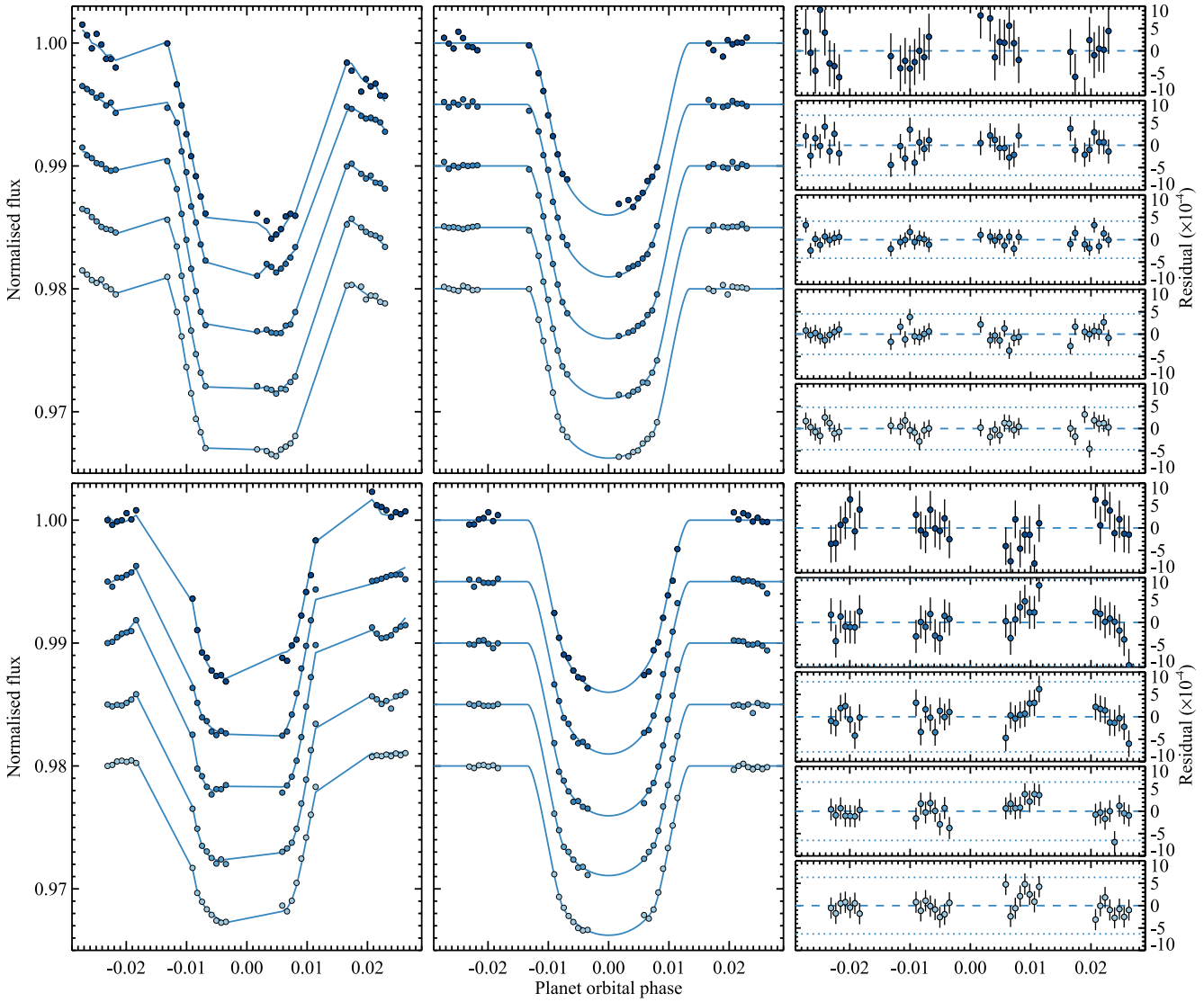

Figure 8. *HST*/STIS G430L observations on UT 2012 May 26 (visit 7) and September 19 (visit 8), top and lower three panels, respectively. Left-hand panels: raw light curves and the best-fitting transit radius, multiplied in flux by a systematics model for each spectral bin, shifted with an arbitrary constant for clarity. Middle panels: corrected light curves and best-fitting transit model. Right-hand panels: observed minus computed residuals with error bars compared to a null level. A 3σ level is indicated with dotted lines.

Model selection was performed similar to grating G430L, attempting the four analytical models for systematics (see Table A1 for details). At each trial, we constructed the transmission spectrum of HAT-P-1b in terms of R_p/R_*. Overall, the spectrum remained quite similar in shape and each measurement varied within 1σ throughout the model selecting process. The BIC statistic was minimized for Model 2. We therefore performed the detrending of each bin of the G750L grating with that model. Similar to the analyses of the transmission spectrum of G430L, we also experimented with shifted spectral bins (±50 Å) to secure stability of the derived spectrum and found good agreement between the R_p/R_* measurements from the three trials. Comprehensively, we did not find a significant difference between χ^2 values originating from the fits based on the 1D against 3D limb darkening coefficients due to the longer wavelengths covered by the G750L grating, where the variation of the limb darkening with wavelength is noticeably weaker. However, for clarity and consistency we report the results using the 3D models.

STIS fringe corrected versus uncorrected time series were employed to investigate the impact of the fringe effect on the resulting transmission spectra. Similar to Knutson et al. (2007) we found that the fringe effect do not influence significantly the transmission spectrum when using large bin sizes (such as our three reddest bins). We choose to report the G750L transmission spectrum based on the fringe corrected data for clarity and consistency.

The transmission spectrum is marginally flat with increasing absorption longward of ∼8500 Å and a deviation of the bin that brackets the sodium feature. As we describe in detail this part of the analysis in Section 3.2.3, we emphasize that we report the wavelength range $\lambda = 5290$–6500 Å of the spectrum with the results from the sodium search. The final version of the G750L spectrum is summarized in Table 6 and Fig. 9. The raw and corrected light curves used to construct the transmission spectrum along with the residuals are exhibited in Fig. 10.

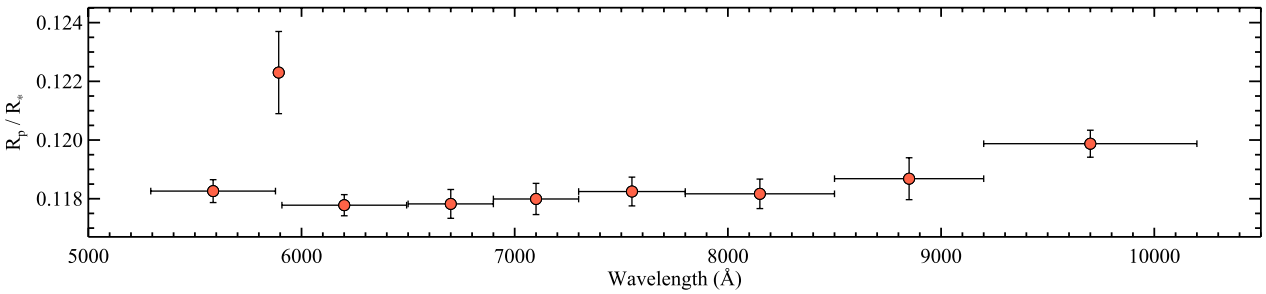

Figure 9. STIS G750L transmission spectrum of HAT-P-1b.

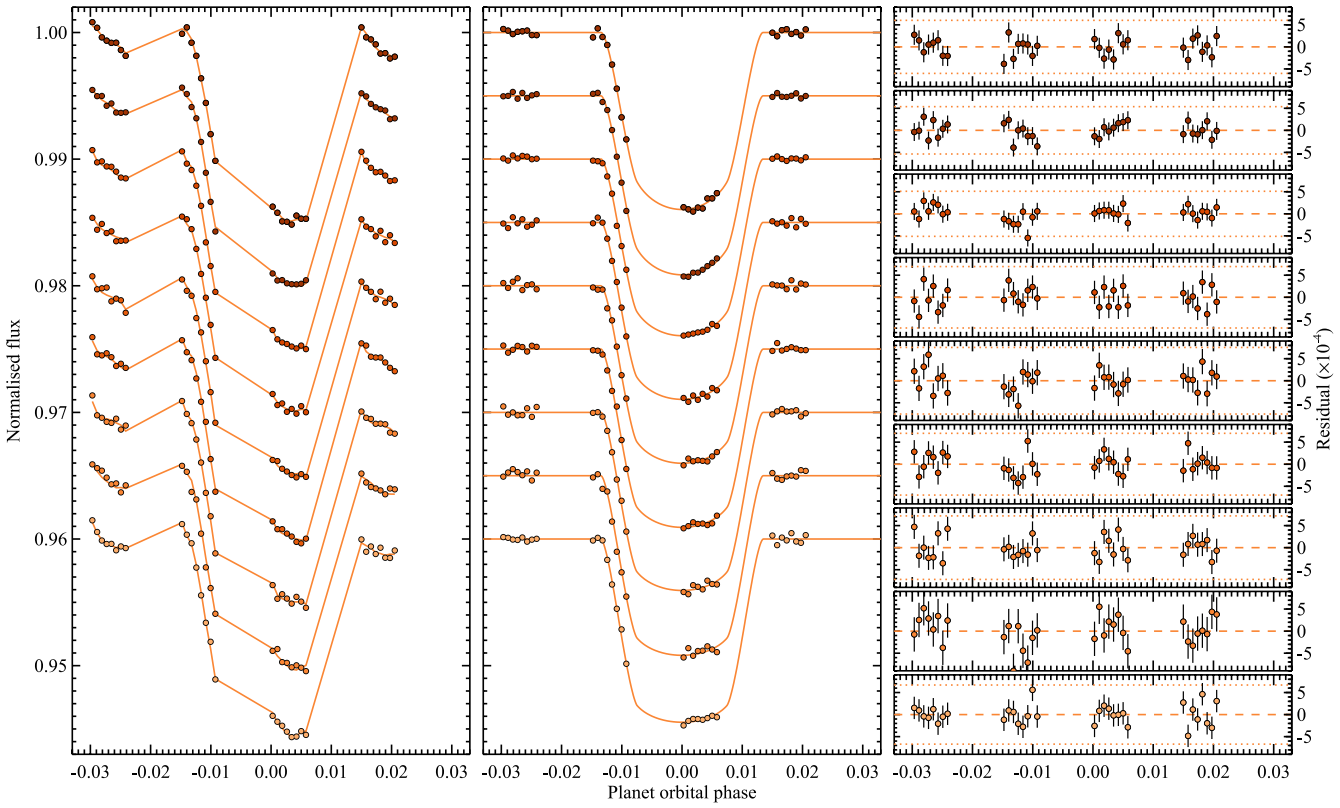

Figure 10. Same as Fig. 8, but for the *HST*/STIS G750L data, obtained on UT 2012 May 30 (visit 20).

3.2.3 Sodium

The most readily identifiable feature in the optical transmission spectrum of HAT-P-1b is the sodium Na I doublet. We pursued the sodium signature employing the differential light-curve procedures described in Charbonneau et al. (2002), Sing et al. (2008b) and Huitson et al. (2012). In summary, we first produced raw photometric time series summing the detected counts over spectral bins, which were then corrected for systematics, that depend on the *HST* orbital phase (fourth-order polynomial) and a linear time term (t). The detection of the individual lines of the sodium resonance doublet ($\lambda_{\rm Na\,I} = 5890$ Å and $\lambda_{\rm Na\,II} = 5896$ Å), separated only by $\sim$6 Å is hampered by the small scale of the STIS instrument ($\sim$5 Å pixel^{-1}) at low spectral resolution ($R = 500$). In addition, the precise width of the feature we seek is unknown. We therefore, select bands of varying width, each centred on the sodium doublet ($\lambda_{\rm Na} = 5893$ Å), aiming similar to Charbonneau et al. (2002) to span 'narrow', 'medium' and 'wide' wavelength regions. However, instead of using three bands we choose to perform a more detailed investigation of the evolution of the detection/non-detection of the sodium feature. The set of bands centred on the sodium feature are 15, 30, 45, 60, 75 and 90 Å wide. We also coupled each of these bands with 'blue' and 'red' bands with a width of 600 Å, in order to bracket the 'centre' band. We selected the out-bands to be significantly wider compared to the in-bands to secure stability of these reference measurements. We further produced photometric time series for each of these 18 bands as described in Section 3.2.2. To investigate for the sodium feature we first computed the mean light curve of the blue '$b(t)$' and red '$r(t)$' bands and subtracted that light curve from the light curve of the centre '$c(t)$' band: $D_{\rm Na}(t) = c(t) - [b(t) + r(t)]/2$, where $D_{\rm Na}(t)$ is the differential light curve. As pointed out by Charbonneau et al. (2002), the advantage of this linear combination is that it removes most of the variations due to the colour dependence of the limb darkening of the stellar continuum. We then computed the difference in the mean of the in- and oot data (indicated by the relevant subscripts): $\Delta D_{\rm Na} = \overline{D_{\rm Na}(t_{\rm in})} - \overline{D_{\rm Na}(t_{\rm out})}$. To estimate an uncertainty of the $\Delta D_{\rm Na}$ differences, we computed the standard deviation of the

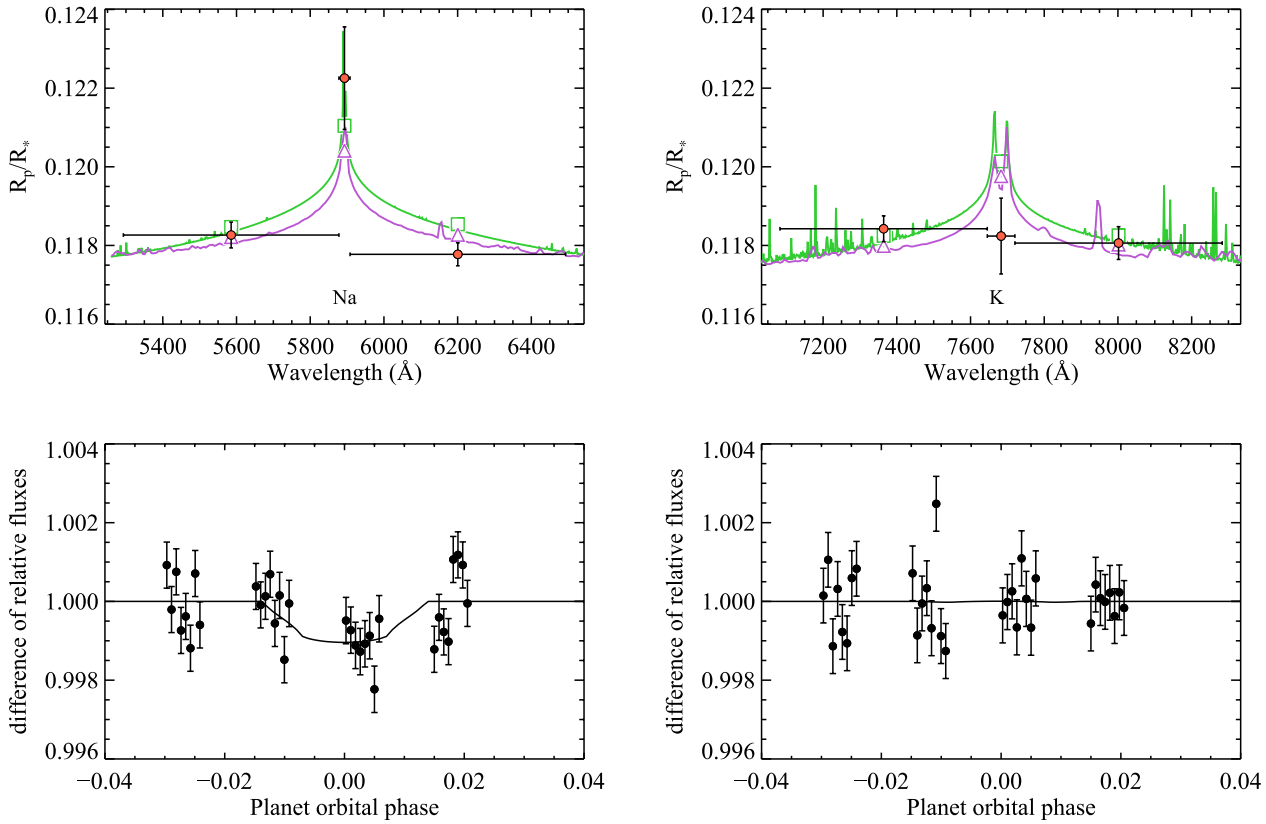

Figure 11. Top panels: the observational transmission spectrum (in terms of R_p/R_* obtained from light-curve fits, shown with dots and vertical error bars; horizontal errors indicate the band widths used to obtain light curves) around the sodium and potassium features (left- and right-hand panels, respectively), compared to theoretical cloud free models [shown with green and purple continuous lines for Fortney et al. (2008, 2010) and Burrows et al. (2010) and Howe & Burrows (2012), respectively, described in detail in Section 4] and the related radius predictions (boxes and triangles), both shifted from each other and the data for clarity. Lower panels: differential-transit light curves of 30 and 75 Å bands, centred on the sodium and potassium doublets, respectively, to that of a reference composed from the average of a blue and red band, bracketing each feature. Differential limb darkening curves are indicated with continuous lines.

mean, Bevington & Robinson (2003). Following this procedure, we found that the sodium feature is detected in each of the six bands with a significance ranging as low as 1.2σ for the 45 Å band to as high as 3.3σ for the 30 Å band. We therefore report the exact values for the highest detection significance: $\Delta D_{\rm Na} = (-98 \pm 30) \times 10^{-5}$. Furthermore, for the six central bands, starting with the narrowest to the widest we observe a monotonic decrease of the measured standard deviation of the oot data. These values are close to the predictions of photon noise-limited precision.

We also used the aforementioned procedure with six bands and scanned the wavelength region $+/-50$ Å from the sodium resonance line in steps of 5 Å, which is close to the resolution of the STIS instrument. Sodium was detected only in the 30 Å region, centred on $\lambda_{\rm Na} = 5893$ Å and most significantly (i.e. strongest signal) when using the narrow bands. In addition, no signal was detected when we moved the bands more than $+/-30$ Å away from the sodium resonance line. Although, the differential procedure significantly decreases the contribution of the stellar limb darkening to the variation of the transit depth, we must also quantify how much of the observed decrement is a result of the distinctive limb darkening exhibited by the sodium line relative to the adjacent continuum, calculating the differential limb darkened transit light curves. As evident in Fig. 11 (lower-left panel) the modelled differential time series shows only weak residual limb darkening effects.

In addition to the positive result from the differential method, we also detected the sodium feature by comparing the measured planet radii from individual fits of transit and systematics models (as in Section 3.2.2) to the six raw light curves from the blue, centre and red bands, respectively. This result is not surprising, given the accurate prediction of the stellar limb darkening, based on 3D atmospheric models. Fig. 11 (left-hand panels) summarizes the sodium detection from both approaches described above.

Based on the result for a significantly deeper transit in the sodium band (3.3σ) compared to the adjacent red and blue bands and the negligible contribution of the residual limb darkening, we conclude that we have detected sodium in the planetary atmosphere of HAT-P-1b.

3.2.4 Potassium and Hα

We followed the two methods, described in Section 3.2.3 to inspect the STIS data for potassium. Because the potassium spectral signature is known to be formed by a doublet, centred at $\lambda_{\rm K} \approx 7684$ Å with two cores separated by 34 Å, we first employed only the set of medium and wide bands, i.e. 45, 60, 75 and 90 Å, centred at $\lambda_{\rm K}$. Each of the four bands showed no detection of transit-depth decrement due to potassium when applying both methods. We therefore report the result for the 75 Å wide band that brackets the doublet: $\Delta D_{\rm K} = (1 \pm 28) \times 10^{-5}$ (see the right-hand panels in Fig. 11). The

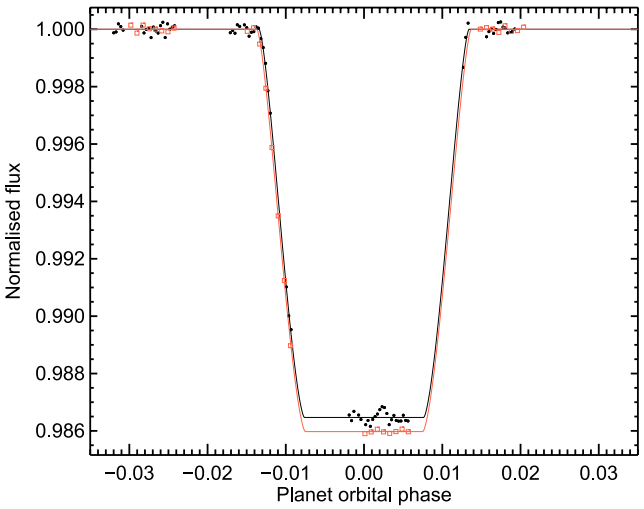

Figure 12. An empirical demonstration of the transit depth difference between the red STIS (boxes) and WFC3 (dots) limb darkening corrected white light curves and transit models (continuous lines). The difference is obvious in each transit exposure, including the ingress.

oot data resulted in standard deviation of 6.4×10^{-4} which is close to the expectation of photon noise-limited precision. We further investigated each of the potassium cores individually with the complete set of bands, i.e. including the two narrow ones. In the case of $\lambda_{\mathrm{K}\,D2} = 7667$ Å, we find no evidence of a significant variation in the transit depth, with the highest value at the 60 Å wide band with $\Delta D_{\mathrm{K}\,D2} = (-25 \pm 24) \times 10^{-5}$ and limb darkening also consistent with no variation: $\Delta D_{\mathrm{ld}} = (12 \pm 16) \times 10^{-5}$. The second core $\lambda_{\mathrm{K}\,D1} = 7701$ Å also gave results consistent with no variation, indicating no presence of potassium. Based on these results, we therefore conclude that there is no evidence in our data for the presence of potassium in the atmosphere HAT-P-1b.

We also inspected the red STIS data for extra absorption in Hα line (6563 Å), following the aforementioned approach. We found no variation of the transit depth at that wavelength.

3.2.5 Transmission spectra level differences

We complement the blue and red STIS transmission spectra discussed in this work with the recently reported near-infrared transmission spectrum of HAT-P-1b by Wakeford et al. (2013), which shows a significant absorption above the 5σ level, matching the 1.4 μm water absorption band. To secure a uniform analysis of the STIS and WFC3 transmission spectra, we coordinated our efforts with Wakeford et al. (2013) and employed the same values for the semimajor axis (a/R_*), orbital period (P) and inclination (i), as described in Section 3, in conjunction with limb darkening coefficients derived from the 3D stellar atmosphere models. Despite the uniform analysis, the level of the optical (blue and red) spectrum seem to be significantly higher than the near-infrared spectrum (Fig. 12). Based on current giant planet atmospheric models, including Burrows et al. (2010) and Howe & Burrows (2012) or Fortney et al. (2008, 2010), described in detail in Section 4, the water feature is expected to peak higher than the base of the wings of the sodium and potassium resonance doublets (see Figs 14 and 13). Surprisingly, in the case of HAT-P-1b the water feature peaks nearly at the level of the wing bases of the sodium and potassium doublets (see R_p/R_* for systematic models 2 and 3 for the red STIS and the WFC3 data, respectively, in Table A1 in the appendix or Table 3). Clearly, an alternative statement can be formulated presuming a higher optical level compared to a low water feature. Regardless the choice of formulation, however, a fundamental question can be raised about the possible shifts in altitude between the three transmission spectra. One speculation for the observed difference could be attributed to stellar activity and spot crossing events. However, based on our stellar activity monitoring (see Section 2.2) we see no evidence in our monitoring data (Fig. 2 with Ca II H&K chromospheric line emission index of $\log R'_{\mathrm{H\&K}} = -4.984$, Knutson, Howard & Isaacson 2010) for variability of HAT-P-1 above ±0.5 per cent (a scatter of 2 mmag consistent with the photometric noise), which is also compatible with the low chromospheric activity concluded in Bakos et al. (2007) and the fact that we do not observe any spot crossings during the transits. This hypothesis hence, cannot explain the observed difference of $4.3 \pm 1.6\,H$, where $H = 414$ km is the assumed scaleheight of HAT-P-1b. Another explanation for the observed difference could be a systematics in the data reduction stage. To help test this hypothesis and to place an absolute uncertainty on the levels of the transmission spectra we investigated the variation of the white light R_p/R_* measurements (including the known correlation of R_p/R_* with a/R_* and i), as we varied a/R_* and i within their best-fitting values with uncertainties (see Section 3.1). In particular, while keeping a/R_* as a free parameter, we fixed the value of the orbital inclination (i) to its lower and upper limits and obtained two radius estimates. The same approach gave two radius estimates when fixing a/R_* and varying i. We then fixed both a/R_* and i to their upper and lower values, respectively, and obtained another two radius estimates; the final two estimates were obtained while keeping one of the parameters to its low/high value while fixing the other to its high/low value.

Using the eight R_p/R_* estimates for each grating/grism, we further computed their mean and standard deviation values (see Table 7). Two interesting facts can be established after an inspection of Table 7. First, the WFC3 data result in a significantly lower R_p/R_* value, compared to the STIS data. In fact, we also investigated the influence of the differential (with respect to HAT-P-1 B companion star) versus single flux white light curve obtained from the WFC3 data. Both results for R_p/R_* were found in good agreements (within their uncertainties) with slightly higher value from the differential light curve; and secondly, contrary to our results at the systematic model selection stage (see Table A1 in the appendix), the WFC3 white light curve showed the smallest spread in R_p/R_*, followed by the red and blue STIS data. We estimate the differences (γ) between the mean R_p/R_* levels for each of the three possible pairs of gratings/grisms of Table 7 and report them in Table 8. We estimated the related uncertainty by propagating the mean uncertainties (based on the eight R_p/R_* estimates) for each grating/grism. While both STIS data sets were found to be in agreement, our results imply a significant difference between the STIS and WFC3 data at a 3σ level.

4 DISCUSSION

Placed together, the blue and red STIS transmission spectra exhibit several noticeable features. Based on the two methods, described in Sections 3.2.3 and 3.2.4, we conclude that we detected sodium (at the 3.3σ level at $\lambda = 5893$ Å), but no excess absorption due to potassium nor Balmer Hα (at $\lambda = 7683$ and 6563 Å, respectively) in the HAT-P-1b planet atmosphere. The blue spectrum exhibits a gradual increase towards shorter wavelengths, while the red spectrum is marginally flat with an enhanced absorption beyond ∼8500 Å. In what follows, we discuss the astrophysical implications of the

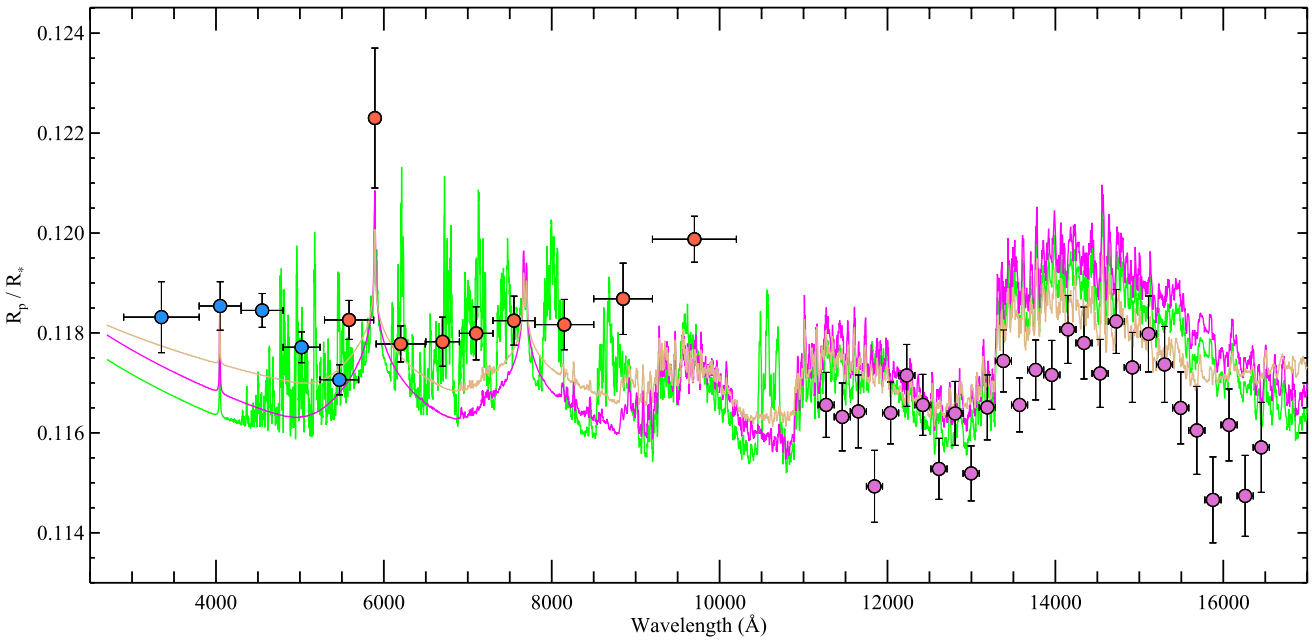

Figure 13. *HST* transmission spectrum (blue, red and purple dots refer to the STIS G430L, G750L and WFC3 data, respectively) compared to atmospheric models (continuous lines) generated for the HAT-P-1 system. Fortney et al. (2008, 2010) isothermal hydrostatic uniform abundance models with an equilibrium temperature 1000 K (brown line) and 1500 K (green line with TiO and VO; purple line: without TiO and VO). Horizontal and vertical error bars indicate the spectral bin sizes and the R_p/R_* uncertainties, respectively.

individual and combined STIS and WFC3 transmission spectra on HAT-P-1b's planetary atmosphere.

4.1 Comparisons to existing theoretical models

The complete optical to near-infrared transmission spectrum was compared to two different sets of atmospheric models, similar to the analysis of Wakeford et al. (2013) and Huitson et al. (2013). One set based on the formalism of Burrows et al. (2010) and Howe & Burrows (2012) and the other, based on the formalism of Fortney et al. (2008, 2010). Our choice to employ two independently derived sets of atmospheric models is governed by the fact that not all model sets in the literature agree, as they were computed using different methods (see Shabram et al. 2011 for details). To perform a comparison between theory and observation we employed pre-computed models and proceeded as follows. From each model, we averaged the model within the wavelength bins that were used to construct the observational transmission spectrum of HAT-P-1b (as detailed in Table 6). Then the pre-computed models were fitted to the data with a single free parameter that controls their vertical position, i.e. without any influence on the model shape. For each model, we computed the χ^2 statistic to quantify model selection. As the models are pre-computed, the number of degrees of freedom at this stage of the analysis is constant for each model, i.e. d.o.f. $= n - m$, where n is the number of data points (see the following text for each sets of models) and m is the number of fitted parameters, i.e. $m = 1$. The comparisons help to test the underlying model assumption (e.g. the presence/absence of TiO) and identify atmospheric species in the transmission spectrum.

Table 7. Mean and standard deviation values of R_p/R_* obtained while varying a/R_* and i.

Data set	$\langle R_p/R_* \rangle$	Deviation
Visit 7/G430L	0.1192	0.0011
Visit 20/G750L	0.118 26	0.000 57
Visit 8/G430L	0.1181	0.0011
Visit 26/G141	0.116 65	0.000 20

Table 8. Transmission spectra level differences.

Grating/grism pair	$\gamma = R_{p1}/R_* - R_{p2}/R_*$
G430L–G750L	$0.000\,37 \pm 0.000\,79$
G430L–G141	$0.001\,97 \pm 0.000\,77$
G750L–G141	$0.001\,61 \pm 0.000\,53$

The models from Burrows et al. (2010) and Howe & Burrows (2012) were specifically generated for the HAT-P-1 system using a 1D dayside temperature–pressure (T-P) profile with stellar irradiation, in radiative, chemical and hydrostatic equilibrium. Chemical mixing ratios and corresponding opacities assume solar metallicity and local thermodynamical chemical equilibrium accounting for condensation with no ionization, using the opacity data base from Sharp & Burrows (2007) and the equilibrium chemical abundances from Burrows & Sharp (1999) and Burrows et al. (2001).

The models based on Fortney et al. (2008, 2010) were also specifically generated for the HAT-P-1 system and included a self-consistent treatment of radiative transfer and chemical equilibrium of neutral and ionic species. Chemical mixing ratios and opacities assume solar metallicity and local chemical equilibrium, accounting for condensation and thermal ionization though no photochemistry (Lodders 1999, 2002, 2009; Lodders & Fegley 2002, 2006; Visscher, Lodders & Fegley 2006; Freedman, Marley & Lodders 2008). In addition to isothermal models, transmission spectra were calculated using 1D T-P profiles for the dayside, as well as an overall cooler planetary-averaged profile. Models were also generated both with

and without the inclusion of TiO and VO opacities. Because each of the aforementioned models started at wavelength $\lambda = 3500$ Å (due to a restriction of the employed opacity data base), we extrapolated the models in the range 2700−3500 Å to enable self-content comparisons to the bluest STIS measurements along with all models.

To compare the standard theory with observation, we first employed Burrows et al. (2010) and Howe & Burrows (2012) dayside model in hydrostatic equilibrium at solar metallicity without TiO/VO and the dayside averaged model of Fortney et al. (2008, 2010). Although both models were pre-computed for the system parameters of HAT-P-1, assuming cloudless atmosphere, they resulted in poor fits. The dayside averaged model of Fortney et al. (2008, 2010) produced the lowest $\chi^2 = 231$, followed by the model of Burrows et al. (2010) and Howe & Burrows (2012) $\chi^2 = 311$ with 41 degrees of freedom (see Fig. 14).

A comparison of the observed transmission spectrum was also carried out to isothermal hydrostatic uniform abundance models of Fortney et al. (2008, 2010) with two equilibrium temperature regimes, different from the one of HAT-P-1b (i.e. ∼1200 K). Such analysis helps provide a general understanding of the observed features as well as any departures from them. The first regime included isothermal models with equilibrium temperature of $T_{\rm eq} = 1500$ K (to represent the hotter dayside) with and without TiO/VO. The second regime included a model at lower equilibrium temperature $T_{\rm eq} = 1000$ K that represents a cooler terminator and not containing TiO/VO. The fit to the $T_{\rm eq} = 1000$ K isothermal model is the best from the three isothermal models fitted to the data, with $\chi^2 = 168$ and 41 degrees of freedom (see Fig. 13). In fact, a temperature of 1000 K is also consistent with the result from Wakeford et al. (2013). The TiO/VO containing model gave a lower χ^2 than the non-TiO/VO model ($\chi^2 = 218$ and 324, respectively), because of the enhanced absorption of the TiO/VO model in the range $\lambda \sim 4000-9000$ Å (see Fig. 13). The presence of TiO/VO has to be further investigated, as the enhanced absorption in the observed spectrum behaves differently than the theoretical expectation. To test this hypothesis, we employed the 'comb' filter described in Huitson et al. (2013) and checked for the presence of TiO features. In summary, the filter is a comb of 'in-TiO' and 'out-TiO' bands, which is sensitive to the smaller features within the large TiO signature in the optical region. The same bands were applied to the two isothermal hydrostatic models (with and without TiO/VO) with an equilibrium temperature $T_{\rm eq} = 1500$ K and surface gravity 10 m s^{-2} and theoretical values derived to compare with the differential measurements from our data. Following this approach, we found a differential absorption depth, scaled to $H = 414$ km, of $\Delta z/H = 0.16 \pm 0.69$ from the data and theoretical values for the TiO and non-TiO models were 0.94 and 0.44, respectively. Since the observational result is consistent with no variation, closer to the theoretical value of the non-TiO model, and the overall fit is rather poor, we conclude that the TiO model is not consistent with the data.

An attempt to perform a better fit to the data was also done incorporating isothermal models, pre-computed for the HAT-P-1b case (see Fig. 14), however, with additional parametric adjustments. First, an unknown 'extra absorber' at altitude of constant optical opacity 0.03 cm^2 g^{-1} (from 4000 to 10000 Å) was incorporated to the isothermal model of Burrows et al. (2010). The extra absorber, whatever its nature, increases the ratio of the optical to infrared radii, which is similar to the wavelength dependent radius variation in the STIS and WFC3 results and has been used to interpret *Spitzer* secondary eclipse observations (Burrows et al. 2007). In addition, the sodium abundance was increased by a factor of 10^3 to potentially represent the sodium detection measurement in the spectral bin 5878−5908 Å. Decreasing the degrees of freedom with 2, due to the two adjustments in the model, we found that this specific model is an improved fit to the data with $\chi^2 = 105$ and 39 degrees

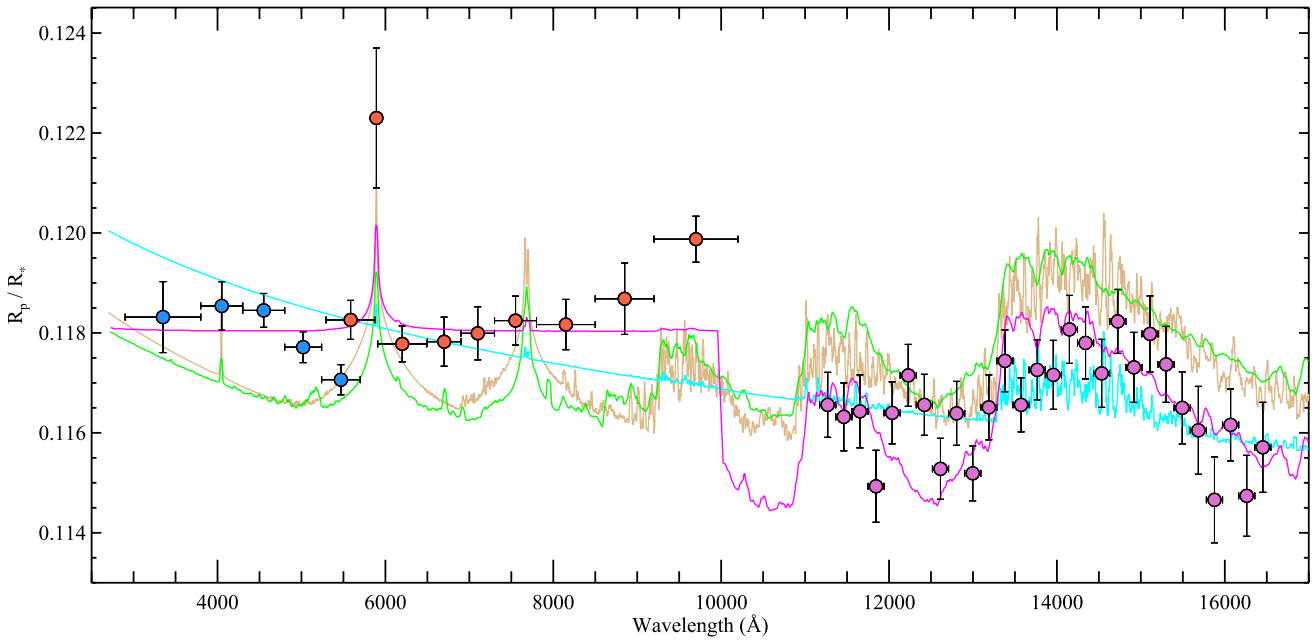

Figure 14. Same as Fig. 13, but for the models assuming specific pressure–temperature profiles and isothermal models with additional adjustments. Green line: dayside model from Burrows et al. (2010) and Howe & Burrows (2012) at solar metallicity without TiO/VO. Brown line: dayside model from Fortney et al. (2008, 2010) without TiO/VO. Purple line: an isothermal model of Burrows et al. (2010) with an 'extra absorber' at altitude with an opacity of 0.03 cm^2 g^{-1} from 0.4 to 1.0 μm. Cyan line: isothermal model from Fortney et al. (2008, 2010) with enhanced (factor of 10^3) Rayleigh scattering. Horizontal and vertical error bars indicate the spectral bin sizes and the $R_{\rm p}/R_*$ uncertainties, respectively.

of freedom (see Fig. 14). The model however, cannot adequately reproduce the enhanced absorption in the bluest and reddest parts of the transmission spectrum (i.e. at decreasing wavelengths shorter than $\lambda \leq 5500$ Å and longer than $\lambda \geq 8500$ Å), as it assumes uniform absorption. Furthermore, even with the enhanced super sodium content the model sodium line prediction seems to be a rather poor match to the observational result. For consistency, we also fitted the theoretical models after ignoring the reddest data points of the blue and red transmission spectra. In these cases, the χ^2 decreased significantly down to 66 for 37 degrees of freedom.

Secondly, the HAT-P-1b isothermal model of Fortney et al. (2008, 2010) was adjusted with an enhanced (factor of 10^3 more) Rayleigh scattering in order to reproduce the observational result. This model resulted in $\chi^2 = 122$ and 40 degrees of freedom (see Fig. 14). However, incorporating more intense Rayleigh scattering seems to mask/suppress the sodium feature. Removing the two reddest outliers the χ^2 decreased to 66 for 39 degrees of freedom.

While the list of theoretical models presented in this study is diverse it is far from complete. An optical absorber/scattering may be needed to explain HAT-P-1b's optical to near-infrared transmission spectrum, as suggested by the models of Burrows et al. (2010) and Fortney et al. (2008, 2010) discussed in the last two paragraphs, respectively. However, these two scenarios will be put into future test with further theoretical models attempting to explain our data and to further constrain HAT-P-1b planetary atmosphere.

4.2 The optical blue transmission spectrum

The G430L transmission spectra derived from a weighted average of individual fits and a simultaneous modelling are found to be in very good agreement (see the lower panel of Figs 6 and 7). The main overall property of the transmission spectrum, in the range 2900–5700 Å, is a relatively smooth featureless slope, analogous to the gradual increase of the absorption with decreasing wavelength in the optical transmission spectrum of HD 209458b (Sing et al. 2008b, also see Ballester, Sing & Herbert 2007; Barman 2007). Contrary to the high-altitude atmospheric haze in HD 189733b, reported in Pont et al. (2008) and Sing et al. (2011b), the feature discussed here of HAT-P-1b is pronounced in the blue grating only, which significantly differs from the case of HD 189733 b, where the feature dominates the complete optical to near-infrared wavelength regime (3000 to 10 000 Å). Based on the simultaneous fit, the value for the slope is found to be 2100 ± 672 km over a wavelength range from 2900 to 5700 Å. Lecavelier Des Etangs et al. (2008) showed that the effective altitude (z) of an exoplanet atmosphere (for a given atmospheric structure and composition) at a wavelength λ and assuming a power law for the cross-section of the scattering particles of the form $\sigma = \sigma_o(\lambda/\lambda_o)^{\alpha}$ (where α is the index for the scattering law) is given by the following expression:

$$z(\lambda) = \frac{kT}{\mu g} \ln\left(\frac{\xi_{\rm abs} P_{\rm o}}{\tau_{\rm eq}} \sqrt{\frac{2\pi R_p}{kT\mu g}}\ \sigma_{\rm o}\left(\frac{\lambda}{\lambda_{\rm o}}\right)^{\alpha}\right), \quad (7)$$

where k is Boltzmann's constant, T is the atmospheric temperature, μ is the mean molecular weight of the atmospheric particles, g is the surface gravity, $\xi_{\rm abs}$ is the abundance of the dominant absorbing species, $P_{\rm o}$ is the pressure at the reference altitude and $\tau_{\rm eq}$ is the optical depth at the transmission spectral radius. Following the discussion of Lecavelier Des Etangs et al. (2008) the slope of the planet radius as a function of the wavelength ($\mathrm{d}z/\mathrm{d}\ln\lambda = \mathrm{d}R_{\rm p}/\mathrm{d}\ln\lambda$) can be derived taking a derivative of z in equation (7) with respect to the logarithm of the wavelength λ:

$$\frac{\mathrm{d}z}{\mathrm{d}\ln\lambda} = \alpha\frac{kT}{\mu g} = \alpha H \Rightarrow\ \alpha T = \frac{\mu g}{k}\frac{\mathrm{d}R_{\rm p}}{\mathrm{d}\ln\lambda} = \frac{\mu g}{k}\frac{\mathrm{d}z}{\mathrm{d}\ln\lambda}, \quad (8)$$

with H representing the atmospheric scaleheight, see also Howe & Burrows (2012). We find $\alpha T = -7535 \pm 2411$ K, assuming $g = 877\,\mathrm{cm\,s^2}$. The dayside average brightness temperature of HAT-P-1b has been determined by Todorov et al. (2010) to be $T = 1500 \pm 100$ K, from secondary eclipse observations with *Spitzer*. This is likely too high for our terminator spectra at lower temperatures and lower pressures with the water feature detected in WFC3 data implying a value closer to 1000 K (Wakeford et al. 2013). Assuming this temperature, our result translates to $\alpha = -7.5 \pm 2.4$. The derived value with uncertainty for α opens up a discussion about the chemical composition of the particles causing the absorption signature within the uncertainty band from ≈ -5 to ≈ -10. Generally, and apart from the molecular hydrogen contents, the chemical composition of gases that cause different slopes in the short optical wavelength regimes are not well known. However, in the case of Rayleigh scattering, the predicted value is $\alpha = -4$, which is close to the lowest border of our result as one of the possibilities. It is hence interesting to speculate the possible source of opacity in the atmosphere of HAT-P-1 b particularly in that case. For example, Lecavelier Des Etangs et al. (2008) found $\alpha = -4$ given the observational data and the measured slope in the transmission spectrum of HD189733b and suggested $MgSiO_3$ as a possible source of opacity.

The estimated slope value for HAT-P-1b implies a scattering different from Rayleigh, though it depends on the temperature at the different altitudes, and followup observations will be needed to better characterize this slope.

Ballester et al. (2007) proposed an alternative explanation for the slope of the transmission spectrum of HD 209458b below 4000 Å as a result of absorption in the Balmer lines and continuum by an optically thin layer of excited hydrogen atoms at high altitude in the planetary atmosphere. Given the single measurement comprising the highest uncertainty of our combined blue transmission spectrum (short ward to 4000 Å), it is challenging to put this hypothesis into test given the HAT-P-1b data.

A second alternative explanation to the Rayleigh scattering has been proposed by Barman (2007) who considered an increase of the absorption in the wavelength range below 5000 Å due to atomic lines. The strongest absorption in that wavelength range is expected to be determined mainly by the lines of Ca I, Fe I, Al I and Cr I. The strongest among those lines (Ca I) is expected to be centred around 4230 Å. If the abundance of Ca is high one would expect the presence of the Ca I and quite possible of some of the other lines in the blue transmission spectrum of HAT-P-1b. However, the present spectral bin sizes are much too large (as constrained by the SNR of the data in each spectral bin) to secure a plausible and robust detection of such narrow spectral features.

4.3 The optical red transmission spectrum

The G750L low-resolution transmission spectrum of HAT-P-1b looks marginally flat except for the region around the sodium feature and at wavelength longer than $\lambda \geq 8500$ Å. As discussed in Section 3.2.3 we detect the core of the sodium (Na I) resonance doublet at the 3.3σ significance level when using a narrow 30 Å spectral bin, centred at $\lambda = 5893$ Å. We searched but did not detect the broad line wings of the sodium feature, which are predicted by

both Burrows et al. (2010) and Howe & Burrows (2012) as well as Fortney et al. (2008, 2010) cloud free theoretical models with solar abundance (see Fig. 11). In contrast to the sodium feature the spectrum shows no radius variation around the potassium doublet (K I, $\lambda_{\rm K\,I} = 7665$ Å and $\lambda_{\rm K\,II} = 7700$ Å), which is similar to the case of HD 209458b (Charbonneau et al. 2002; Sing et al. 2008b; Jensen et al. 2011). Furthermore, the spectrum exhibits a gradual increase of the absorption, with increasing wavelength at wavelengths larger than 8500 Å. Huitson et al. (2013) did not find evidence for this effect in the STIS G750L spectral data of WASP-19b, which is part of our survey. Notably, an enhanced absorption is present in the STIS G750L transmission spectrum of HD 209458b reported in Knutson et al. (2007). As HAT-P-1b is the second case after HD 209458b with evidence of enhanced absorption at wavelengths longward to 8500 Å it is likely that the observed effect is real and can be attributed to absorption in these two planetary atmospheres.

4.3.1 The relative sodium abundance

Exoplanet transmission spectra allow the abundances to be determined from identified absorption features. In the case of HAT-P-1b, when two or more signatures are present, the relative abundance can be measured (Lecavelier Des Etangs et al. 2008; Désert et al. 2009; Huitson et al. 2012). HAT-P-1b is only the second case (after HD 209458b) in the atmosphere of which signatures from both sodium and water are conclusively detected with transmission spectroscopy (Charbonneau et al. 2002; Sing et al. 2012; Deming et al. 2013). For HAT-P-1b, the base of the missing sodium wings is higher than the peak of the water feature, and a possible explanation could incorporate an enhanced abundance of sodium in the planet atmosphere.

The relative abundance of the sodium to water, assuming a constant temperature and pressure is given by

$$\frac{\xi_{\rm Na}}{\xi_{\rm H_2O}} = \frac{\sigma_{\rm H_2O}}{\sigma_{\rm Na}} e^{(Z_{\rm Na} - Z_{\rm H_2O})/H}, \quad (9)$$

where $\xi_{\rm Na}$ and $\xi_{\rm H_2O}$ are the abundances, $\sigma_{\rm Na}$ and $\sigma_{\rm H_2O}$ are the wavelength-dependent cross-sections at 5893 Å and 1.4 μm, respectively, and $Z_{\rm Na}$ and $Z_{\rm H_2O}$ are the altitudes of the observed features. However, in the HAT-P-1b case, there is further complication as the individual cores of the sodium doublet are not resolved at the spectral resolution of our data and we also did not find evidence for the presence of pressure-broadened sodium wings. This limitation prevents determination of the pressure level observed in our transmission spectrum, which is degenerate with absolute abundance measurements. It also hampers the modelling of the sodium lines and limits a derivation of temperature with altitude. The temperature also has a small effect on $\sigma_{\rm Na}$. If the temperature is not constant as a function of altitude (z), the abundance measurement will be affected since higher temperatures cause an increase in z for the same cross-section.

To estimate the relative sodium to water abundance ratios, ideally one would employ the measured radii of both species at the same altitude, corresponding to similar temperatures. Although we are prevented of such luxury due to the limitation of the low-resolution data, we provide an abundance measurement assuming that both features occur in atmospheric regions of the same temperature. Using an average scaleheight of 414 km (which assumes a temperature of 1000 K) and similar temperature between the Na and H_2O features, we estimate an upper limit of the sodium abundance compared to water. We assumed water cross-section $\sigma_{\rm H_2O} = 8.9 \times 10^{-22}$ cm^2 based on Sharp & Burrows (2007). To compute the sodium cross-section we followed the approach of Huitson et al. (2012), however, we normalized the integrated cross-section to the stellar spectrum over the 30 Å bin (used to detect sodium in this study), which gave $\sigma_{\rm Na} = 2.3 \times 10^{-20}$ cm^2. Using the derived cross-sections and the measured $R_{\rm p}/R_* = 0.1223 \pm 0.0014$ for the sodium line and $R_{\rm p}/R_* = 0.11631 \pm 0.0003$ for the water feature (see Table 6 and A1, respectively), one finds $\ln(\xi_{\rm Na}/\xi_{\rm H_2O}) = +4.6 \pm 2.2$. For comparison, the solar abundance ratio of sodium to water is $\ln(\xi_{\rm Na}/\xi_{\rm H_2O})_{\rm solar} = -5.0$ to -4.6 (Lodders & Fegley 2002; Lodders 2003; Sharp & Burrows 2007). Despite a large uncertainty, this result indicates an overabundance of sodium compared to water. While we considered an enhanced (factor of 10^3, i.e. $\ln(\xi_{\rm Na}/\xi_{\rm H_2O})_{\rm supersolar} = +2.3$) sodium to water abundance in the specific theoretical model of Burrows et al. (2010) with the 'extra absorber' of uncertain origin, that model was still a rather poor fit to the data. This and additional competing scenarios would be needed to further constrain the atmosphere of HAT-P-1b.

4.4 Interpretation

The complete optical to near-infrared HAT-P-1b transmission spectrum from STIS and WFC3 constraints several important features of the planet atmosphere. First of all, the red STIS spectra show evidence of sodium (3.3σ significance) and lack of potassium. The fact that the sodium cores have been detected but not the wings can potentially be explained by an extra absorber or scatter, which obscures/masks sodium and potassium features (Seager & Sasselov 2000). This is in accord with the lack of any evidence in the STIS G750L data of potassium and the overall marginally flat transmission spectrum, which makes the optical spectrum of HAT-P-1b similar to that of HD 209458b. This is potentially interesting, because both host stars are of similar spectral type and metallicity. One explanation for the lack of potassium, and presence of sodium could be a general underabundance of potassium in the HAT-P-1b atmosphere. Moreover, compared to potassium the sodium atom requires somewhat more energy to ionize. In particular, the first ionization energies for sodium and potassium are $X_{\rm Na} \sim 500$ kJ mol^{-1} and $X_{\rm K} \sim 420$ kJ mol^{-1}, respectively, which can partially explain the presence of sodium and no potassium, if there is significant non-thermal ionization, which is reasonable for highly irradiated planets. Furthermore, the neutral potassium is ∼1.7 times heavier ($m_a = 39$ amu[12]) than the sodium ($m_a = 23$ amu) atom, which may make it harder to vertically mix the species.

The optical STIS data rules out also an atmosphere dominated by high-altitude cloud layer. If it existed, then such hypothetical cloud deck would be expected to block (depending on its properties) the complete optical to near-infrared spectrum. Instead, the spectrum exhibits two opposite slopes and a sodium line core in the optical and water feature in the near-infrared.

A comparative analysis of the data with theoretical models of Fortney et al. (2010) shows that an atmosphere dominated by TiO in the optical regime could hardly explain the optical STIS results. This is no surprise given the medium equilibrium temperature of HAT-P-1 is ∼1000–1300 K, which is expected not be able to sustain gaseous titanium and vanadium oxides. These compounds are expected to rain down in solids at these temperatures and hence such gases are not expected to determine the opacity in the optical regime. Compared to the water feature in the near-infrared, the STIS optical spectrum has much higher overall opacity. The observed offset cannot be explained as due to stellar activity of the host star nor as

[12] amu – atomic mass unit.

a result of the non-linearity of the WFC3 detector. A reason for the second case is that the WFC3 spectra were obtained well within the linear regime of the camera. Finally, adopting a uniform analysis of the STIS and the WFC3 data sets we also rule out a calibration error as a potential explanation for the observed offset. We are hopeful that near-future observations of the HAT-P-1b system may further glean more evidence for the difference between the optical and near-infrared transmission spectra. While the theoretical model of Burrows et al. (2010) with unknown extra absorber and an increased (factor 10^3) sodium to water abundance ratio is a step in improving the fit to the HAT-P-1b STIS and WFC3 data, this scenario would be tastable along with additional competing scenarios. If confirmed, it would suggest that the HAT-P-1b atmosphere is dominated by an absorber in the optical, partially blocking the sodium wings and completely masking the potassium feature, yet leaving an unmuted water feature at 1.4 μm.

5 CONCLUSION

In this paper, we report *HST*/STIS transmission spectroscopy of the transiting hot Jupiter HAT-P-1 b, during two transits with the G430L grating (2900–5700 Å) and one transit with G750L grating (2900–5700 Å). The present STIS results are the third (from a large *HST* survey of eight transiting hot Jupiters) after those of Huitson et al. (2013) who reported on WASP-19b and Wakeford et al. (2013) on HAT-P-1b with WFC3. We refine significantly the system physical parameters and HAT-P-1b's orbital ephemeris and derive the optical to near-infrared transmission spectrum of the planet. We combine this spectrum with the recently reported WFC3 data by Wakeford et al. (2013) to constrain the planetary atmospheric properties.

The STIS G750L transmission spectrum is marginally flat, showing evidence for the presence of the sodium (Na I) resonance line. We detect the core of the sodium resonance doublet at the 3.3σ significance level and find no evidence for the presence of sodium pressure-broadened wings. Despite its wider nature, compared to sodium, we find no evidence for the potassium feature in the low-resolution STIS data.

The STIS G430L spectrum shows an increasing absorption shortward to 5300 Å. The measured slope $\alpha = -7.5 \pm 2.4$ (assuming brightness temperature $T = 1000$ K) spans a range of possible scattering signatures approaching Rayleigh (i.e. a slope with $\alpha = -4$) at the lower limit of our measurement. However, more clarification and constraints can be derived with additional followup data, that would increase the accuracy of the derived slope.

Given these characteristics the optical transmission spectrum of HAT-P-1b seems analogous to HD 209458b in many ways. However, a significant difference between both is that HAT-P-1b contains only a core of the sodium line, while HD 209458b shows broad line wings and extra absorption shortward of the sodium central line.

After a uniform analysis of the white light curves, we combined our STIS spectrum with the spectrum of Wakeford et al. (2013), exhibiting the 1.4 μm water signature. The flat optical STIS spectrum is found to show absorption from higher altitudes (at larger planet radius) compared to the WFC3 spectrum ($4.3 \pm 1.6H$), implying strong optical absorption higher in the atmosphere of HAT-P-1b. Further observations are required to confirm this result. Attempting a range of theoretical cloud free atmospheric models of hot Jupiter exoplanets, including these presented in Burrows et al. (2010) and Howe & Burrows (2012) and Fortney et al. (2008, 2010), specifically pre-computed for the system parameters of HAT-P-1b, we found poor fits to the data.

The Burrows et al. (2010) and Howe & Burrows (2012) HAT-P-1b isothermal model with unknown 'extra absorber' at altitude of constant optical opacity $0.03\,\mathrm{cm^2\,g^{-1}}$ (from 4000 to 10 000 Å) and enhanced sodium abundance (by a factor of 10^3 compared to water) is one scenario that could explain the difference between STIS and WFC3 transmission spectrum. However, this model is unable to reproduce the enhanced absorption in the blue and red STIS spectrum. Further modelling incorporating additional scenarios would be needed to test the plausibility of this hypothesis. The planetary atmosphere of HAT-P-1b is the second case after HD 209458b and HD 189733b with a conclusive detection of both sodium and water.

ACKNOWLEDGEMENTS

This work is based on observations with the NASA/ESA *Hubble Space Telescope*. We are grateful to the team at the STScI help desk for their roles in resolving technical issues with the STIS data processing pipeline. NN and DKS acknowledge support from STFC consolidated grant ST/J0016/1. CMH and PAW acknowledge a support from STFC grants. All US-based co-authors acknowledge support from the Space Telescope Science Institute under HST-GO-12473 grants to their respective institutions. The authors would like to acknowledge the anonymous referee for their useful comments.

REFERENCES

Bakos G. Á. et al., 2007, ApJ, 656, 552
Ballester G. E., Sing D. K., Herbert F., 2007, Nat., 445, 511
Barman T., 2007, ApJ, 661, L191
Béky B., Holman M. J., Gilliland R. L., Bakos G. Á., Winn J. N., Noyes R. W., Sasselov D. D., 2013, AJ, 145, 166
Berta Z. K. et al., 2012, ApJ, 747, 35
Bevington P. R., Robinson D. K., 2003, Data Reduction and Error Analysis for the Physical Sciences. McGraw-Hill, New York
Brown T. M., Charbonneau D., Gilliland R. L., Noyes R. W., Burrows A., 2001, ApJ, 552, 699
Burrows A., Sharp C. M., 1999, ApJ, 512, 843
Burrows A., Hubbard W. B., Lunine J. I., Liebert J., 2001, Rev. Mod. Phys., 73, 719
Burrows A., Hubeny I., Budaj J., Knutson H. A., Charbonneau D., 2007, ApJ, 668, L171
Burrows A., Rauscher E., Spiegel D. S., Menou K., 2010, ApJ, 719, 341
Charbonneau D., Brown T. M., Noyes R. W., Gilliland R. L., 2002, ApJ, 568, 377
Charbonneau D., Knutson H. A., Barman T., Allen L. E., Mayor M., Megeath S. T., Queloz D., Udry S., 2008, ApJ, 686, 1341
Claret A., 2000, A&A, 363, 1081
Deming D. et al., 2013, ApJ, 774, 95
Désert J.-M., Lecavelier des Etangs A., Hébrard G., Sing D. K., Ehrenreich D., Ferlet R., Vidal-Madjar A., 2009, ApJ, 699, 478
Eastman J., Gaudi B. S., Agol E., 2012, EXOFAST: Fast Transit and/or RV Fitter for Single Exoplanet. Astrophysics Source Code Library
Fortney J. J., Lodders K., Marley M. S., Freedman R. S., 2008, ApJ, 678, 1419
Fortney J. J., Shabram M., Showman A. P., Lian Y., Freedman R. S., Marley M. S., Lewis N. K., 2010, ApJ, 709, 1396
Freedman R. S., Marley M. S., Lodders K., 2008, ApJS, 174, 504
Gilliland R. L., Goudfrooij P., Kimble R. A., 1999, PASP, 111, 1009
Goudfrooij P., Bohlin R. C., Walsh J. R., Baum S. A., 1998a, STIS Instrum. Sci. Rep., STIS Near-IR Fringing. II. Basics and Use of Contemporaneous Flats for Spectroscopy of Point Sources (Rev. A)

Goudfrooij P., Christensen J. A., 1998b, STIS Instrum. Sci. Rep., STIS Near-IR Fringing. III. A Tutorial on the Use of the IRAF Tasks
Grillmair C. J., Charbonneau D., Burrows A., Armus L., Stauffer J., Meadows V., Van Cleve J., Levine D., 2007, ApJ, 658, L115
Hasan H., Bely P. Y., 1993, BAAS, 25, 113.06
Hasan H., Bely P. Y., 1994, in Hanisch R. J., White R. L., eds, The Restoration of HST Images and Spectra - II. Space Telescope Science Institute, Baltimore, p. 157
Hayek W., Sing D., Pont F., Asplund M., 2012, A&A, 539, A102
Howe A. R., Burrows A. S., 2012, ApJ, 756, 176
Huitson C. M., Sing D. K., Vidal-Madjar A., Ballester G. E., Lecavelier des Etangs A., Désert J.-M., Pont F., 2012, MNRAS, 422, 2477
Huitson C. M. et al., 2013, MNRAS, 434, 3252
Jensen A. G., Redfield S., Endl M., Cochran W. D., Koesterke L., Barman T. S., 2011, ApJ, 743, 203
Jensen A. G., Redfield S., Endl M., Cochran W. D., Koesterke L., Barman T., 2012, ApJ, 751, 86
Johnson J. A. et al., 2008, ApJ, 686, 649
Katsanis R. M., McGrath M. A., 1998, STIS Instrum. Sci. Rep., The Calstis IRAF Calibration Tools for STIS Data
Knutson H. A., Charbonneau D., Noyes R. W., Brown T. M., Gilliland R. L., 2007, ApJ, 655, 564
Knutson H. A., Charbonneau D., Allen L. E., Burrows A., Megeath S. T., 2008, ApJ, 673, 526
Knutson H. A., Howard A. W., Isaacson H., 2010, ApJ, 720, 1569
Lecavelier des Etangs A., Pont F., Vidal-Madjar A., Sing D., 2008, A&A, 481, L83
Liu X., Burrows A., Ibgui L., 2008, ApJ, 687, 1191
Lodders K., 1999, ApJ, 519, 793
Lodders K., 2002, ApJ, 577, 974
Lodders K., 2003, ApJ, 591, 1220
Lodders K., 2009, preprint (arXiv:0910.0811)
Lodders K., Fegley B., 2002, Icarus, 155, 393
Lodders K., Fegley B., Jr, 2006, Chemistry of Low Mass Substellar Objects. Springer-Verlag, Berlin, p. 1
Mandel K., Agol E., 2002, ApJ, 580, L171
Markwardt C. B., 2009, in Bohlender D. A., Durand D., Dowler P., eds, ASP Conf. Ser. Vol. 411, Astronomical Data Analysis Software and Systems XVIII. Astron. Soc. Pac., San Francisco, p. 251
Mayor M., Queloz D., 1995, Nat., 378, 355
Narita N. et al., 2005, PASJ, 57, 471
Pont F., Zucker S., Queloz D., 2006, MNRAS, 373, 231
Pont F., Knutson H., Gilliland R. L., Moutou C., Charbonneau D., 2008, MNRAS, 385, 109
Redfield S., Endl M., Cochran W. D., Koesterke L., 2008, ApJ, 673, L87
Schwarz G., 1978, Ann. Stat., 6, 461
Seager S., 2011, Exoplanets. Univ. Arizona Press, Tuscan, AZ
Seager S., Sasselov D. D., 2000, ApJ, 537, 916
Shabram M., Fortney J. J., Greene T. P., Freedman R. S., 2011, ApJ, 727, 65
Sharp C. M., Burrows A., 2007, ApJS, 168, 140
Sing D. K., 2010, A&A, 510, A21
Sing D. K., Vidal-Madjar A., Désert J.-M., Lecavelier des Etangs A., Ballester G., 2008a, ApJ, 686, 658
Sing D. K., Vidal-Madjar A., Lecavelier des Etangs A., Désert J.-M., Ballester G., Ehrenreich D., 2008b, ApJ, 686, 667
Sing D. K., Désert J.-M., Lecavelier des Etangs A., Ballester G. E., Vidal-Madjar A., Parmentier V., Hebrard G., Henry G. W., 2009, A&A, 505, 891
Sing D. K. et al., 2011a, A&A, 527, A73
Sing D. K. et al., 2011b, MNRAS, 416, 1443
Sing D. K. et al., 2012, MNRAS, 426, 1663
Snellen I. A. G., Albrecht S., de Mooij E. J. W., Le Poole R. S., 2008, A&A, 487, 357
Steele I. A., Bates S. D., Gibson N., Keenan F., Meaburn J., Mottram C. J., Pollacco D., Todd I., 2008, Proc. SPIE, 7014
Suchkov A., Hershey J., 1998, Instrum. Sci. Rep. NICMOS, NICMOS Focus and HST Breathing
Todorov K., Deming D., Harrington J., Stevenson K. B., Bowman W. C., Nymeyer S., Fortney J. J., Bakos G. A., 2010, ApJ, 708, 498
Torres G., Winn J. N., Holman M. J., 2008, ApJ, 677, 1324
Torres G., Andersen J., Giménez A., 2010, A&AR, 18, 67
Visscher C., Lodders K., Fegley B., Jr, 2006, ApJ, 648, 1181
Wakeford H. R. et al., 2013, MNRAS, 435, 3481
Winn J. N., 2010, preprint (arXiv:1001.2010)
Winn J. N. et al., 2007, AJ, 134, 1707
Winn J. N. et al., 2008, AJ, 136, 1753
Winn J. N. et al., 2009, ApJ, 693, 794
Wood P. L., Maxted P. F. L., Smalley B., Iro N., 2011, MNRAS, 412, 2376
Zhou G., Bayliss D. D. R., 2012, MNRAS, 426, 2483

APPENDIX A: MODEL SELECTION FOR THE SYSTEMATICS OF THE STIS AND WFC3 WHITE LIGHT CURVES

Table A1 summarizes the results for the relevant competing systematics models, identified using the white light curves of the STIS and WFC3 data sets fitted on individual basis (i.e. not in a joint fit with the remaining data). There are several interesting facts that can be concluded from Table A1. First of all, assuming that the photometric uncertainties for each of the three STIS white light curves are dominated by systematics (given the negligible dark current and read-out noise of the STIS CCD detector) the reduced chi square (χ_r^2) can be used as an indicator for the level of the photon noise of our data. In particular, one can conclude that for the three white light curves the data are at about ∼44–52 per cent of the theoretical photon noise. Certainly, one might doubt that the systematics model could be significantly different from the favoured models in the present analysis. However, the STIS white light curves analysed here show no significant correlations to any of the quantified systematics in order to suggest a functional model for the later. We therefore rely on the lowest BIC values in Table A1 as a model indicator of a systematics function of the STIS data. Compared to the STIS white light curves the BIC behaves significantly different for the WFC3 data. The statistic constantly decreases with increasing number of the orders of the *HST* and planet orbital phases. While we might blindly accept the BIC result and choose model 5 as most appropriate it would be rather hard to point out a physical explanation for the sixth or seventh order *HST* orbital phase (ϕ_t). We therefore assume model 3 as a sufficiently good analytic approximation for the systematics in WFC3.

Another interesting fact that can be concluded from Table A1 is that the individual light-curve fits for visits 7, 8 and 20 as well as the WFC3 show noticeably similar results for the system parameters (a/R_* and i) at the one sigma level, regardless of the applied model for the systematics. The later conclusion is also valid for the estimated transit depths (measured with R_p/R_*) for both G430L data sets for which the measured R_p/R_* values from each visit (separated more than 100 d in time) agree well for a given model. Visit 20 shows one outlier for R_p/R_* (model 1, which is unfavored though) which still differs from the highest value at a rather lower level (1.4σ). However, in the result for WFC3, we observe more than 3.5σ difference between the minimum and maximum values for R_p/R_* (models 3 and 1, respectively). This is an important fact which will be discussed again when we paste the STIS and WFC3 transmission spectra in Section 3.2.5.

Table A1. Model selection of an appropriate function for the systematics in the white light curves of the STIS and WFC3 data.

Model	BIC	χ^2	d.o.f.	n	χ^2_r	i (°)	a/R_*	R_p/R_*	$b = a/R_* \cos i$
STIS G430L (Visit 7)									
1	86	47	21	32	2.26	85.773 ± 0.065	10.006 ± 0.086	$0.118\,17 \pm 0.000\,41$	0.737 ± 0.013
2	88	47	20	32	2.34	85.798 ± 0.072	10.037 ± 0.094	$0.117\,95 \pm 0.000\,48$	0.735 ± 0.014
3	92	47	19	32	2.45	85.806 ± 0.075	10.049 ± 0.099	$0.117\,85 \pm 0.000\,53$	0.735 ± 0.015
4	95	46	18	32	2.60	85.802 ± 0.076	10.04 ± 0.10	$0.117\,86 \pm 0.000\,53$	0.735 ± 0.015
5	98	46	17	32	2.72	85.808 ± 0.092	10.05 ± 0.13	$0.117\,87 \pm 0.000\,61$	0.735 ± 0.019
6	98	43	16	32	2.67	85.819 ± 0.079	10.06 ± 0.10	$0.117\,82 \pm 0.000\,56$	0.734 ± 0.016
7	100	45	16	32	2.82	85.803 ± 0.080	10.04 ± 0.11	$0.117\,83 \pm 0.000\,54$	0.735 ± 0.016
STIS G430L (Visit 8)									
1	82	44	20	31	2.23	85.958 ± 0.080	10.32 ± 0.11	$0.117\,08 \pm 0.000\,43$	0.728 ± 0.016
2	79	38	19	31	1.98	85.894 ± 0.085	10.24 ± 0.12	$0.117\,20 \pm 0.000\,46$	0.733 ± 0.017
3	81	37	18	31	2.04	85.878 ± 0.082	10.22 ± 0.11	$0.117\,19 \pm 0.000\,42$	0.734 ± 0.017
4	83	35	17	31	2.05	85.907 ± 0.088	10.26 ± 0.12	$0.117\,11 \pm 0.000\,43$	0.732 ± 0.018
5	84	32	16	31	2.00	85.900 ± 0.086	10.24 ± 0.12	$0.117\,43 \pm 0.000\,50$	0.732 ± 0.017
6	85	30	15	31	2.00	85.936 ± 0.089	10.32 ± 0.13	$0.117\,03 \pm 0.000\,54$	0.731 ± 0.018
7	87	32	15	31	2.14	85.900 ± 0.084	10.24 ± 0.12	$0.117\,43 \pm 0.000\,48$	0.732 ± 0.017
STIS G750L (Visit 20)									
1	88	50	21	32	2.35	85.542 ± 0.072	9.581 ± 0.077	$0.117\,83 \pm 0.000\,52$	0.745 ± 0.014
2	80	39	20	32	1.94	85.495 ± 0.071	9.618 ± 0.076	$0.118\,43 \pm 0.000\,51$	0.756 ± 0.013
3	83	38	19	32	2.00	85.488 ± 0.071	9.633 ± 0.078	$0.118\,44 \pm 0.000\,53$	0.758 ± 0.013
4	83	35	18	32	1.94	85.483 ± 0.072	9.670 ± 0.081	$0.118\,60 \pm 0.000\,53$	0.762 ± 0.014
5	87	35	17	32	2.03	85.480 ± 0.079	9.667 ± 0.078	$0.118\,64 \pm 0.000\,55$	0.762 ± 0.015
6	88	33	16	32	2.03	85.471 ± 0.075	9.662 ± 0.080	$0.118\,62 \pm 0.000\,54$	0.763 ± 0.014
7	89	34	16	32	2.10	85.536 ± 0.083	9.633 ± 0.080	$0.118\,08 \pm 0.000\,60$	0.750 ± 0.015
WFC3 G141 (Visit 26)									
1	223	179	70	80	2.56	85.529 ± 0.079	9.784 ± 0.091	$0.117\,44 \pm 0.000\,26$	0.763 ± 0.015
2	174	125	69	80	1.82	85.599 ± 0.079	9.790 ± 0.089	$0.117\,23 \pm 0.000\,23$	0.751 ± 0.015
3	164	111	68	80	1.63	85.676 ± 0.083	9.896 ± 0.095	$0.116\,31 \pm 0.000\,30$	0.746 ± 0.016
4	164	107	67	80	1.60	85.662 ± 0.083	9.906 ± 0.097	$0.116\,38 \pm 0.000\,31$	0.749 ± 0.016
5	141	80	66	80	1.21	85.607 ± 0.083	9.853 ± 0.095	$0.116\,73 \pm 0.000\,32$	0.755 ± 0.016
6	144	78	65	80	1.20	85.607 ± 0.083	9.852 ± 0.098	$0.116\,75 \pm 0.000\,32$	0.754 ± 0.016
7	145	75	64	80	1.17	85.598 ± 0.082	9.837 ± 0.096	$0.116\,80 \pm 0.000\,32$	0.755 ± 0.016

Model types for STIS G430L/G750L:

$1 - \phi_t + \phi_t^2 + \phi_t^3 + \phi_t^4 + t$

$2 - \phi_t + \phi_t^2 + \phi_t^3 + \phi_t^4 + t + \omega$

$3 - \phi_t + \phi_t^2 + \phi_t^3 + \phi_t^4 + t + \omega + x$

$4 - \phi_t + \phi_t^2 + \phi_t^3 + \phi_t^4 + t + \omega + x + y$

$5 - \phi_t + \phi_t^2 + \phi_t^3 + \phi_t^4 + t + \omega + \omega^2 + x + y$

$6 - \phi_t + \phi_t^2 + \phi_t^3 + \phi_t^4 + t + \omega + \omega^2 + x + x^2 + y$

$7 - \phi_t + \phi_t^2 + \phi_t^3 + \phi_t^4 + t + \omega + \omega^2 + x + y + y^2$

Model types for WFC3 G141:

$1 - \phi_t + \phi_t^2 + \phi_t^3 + \phi_t^4$

$2 - \phi_t + \phi_t^2 + \phi_t^3 + \phi_t^4 + t$

$3 - \phi_t + \phi_t^2 + \phi_t^3 + \phi_t^4 + t + t^2$

$4 - \phi_t + \phi_t^2 + \phi_t^3 + \phi_t^4 + \phi_t^5 + t + t^2$

$5 - \phi_t + \phi_t^2 + \phi_t^3 + \phi_t^4 + \phi_t^5 + \phi_t^6 + t + t^2$

$6 - \phi_t + \phi_t^2 + \phi_t^3 + \phi_t^4 + \phi_t^5 + \phi_t^6 + \phi_t^7 + t + t^2$

$7 - \phi_t + \phi_t^2 + \phi_t^3 + \phi_t^4 + \phi_t^5 + \phi_t^6 + \phi_t^7 + \phi_t^8 + t + t^2$

This paper has been typeset from a TEX/LATEX file prepared by the author.